Rock Mechanics and Rock Engineering (2022) 55:6339–6365
https://doi.org/10.1007/s00603-022-02932-6

ORIGINAL PAPER

# Experimental and Numerical Analysis of Axially Loaded Bored Piles Socketed in a Conglomerate Rock Mass

**Adis Skejić[1] · Dejan Gavrić[2] · Mario Jurišić[3] · Đani Rahimić[4]**

Received: 20 October 2021 / Accepted: 16 May 2022 / Published online: 29 June 2022


## Abstract

This paper presents the details of an experimental and numerical analysis performed on two 1.0 m and one 0.9 m diameter bored piles socketed in the conglomerate rock mass. The study investigates how shaft and base resistance contribute to load settlement behavior of piles built in poorly and well-cemented conglomerate rock mass. Two of the piles were constructed as complete sockets, and the third one is a shear socket only. The testing procedure included measuring pile cap settlement and deformations along with the pile (telltales and strain gauges). The results indicate that not only well cemented but poorly cemented conglomerate as well can sustain heavy surcharge before settlements indicating the commencement of full slip were reached. Numerical simulation of the socket with explicitly modeled roughness was applied to assess the influence of socket side surface strength on the behavior of the test pile. The parameters of numerical models were derived from back analysis of field pile load test combined with recorded socket side roughness and the strength parameters obtained by the direct shear tests of conglomerate intact specimens. The results were compared with the experimental observations, and a good level of agreement with measurements was confirmed.

## Highlights

- Reports the results of full-scale axially loaded bored piles socketed in a poorly cemented conglomerate rock mass, serving as a benchmark for verifying empirical models for piles of the relevant type.
- Reports the pile shaft roughness data and intact strength of conglomerate rock samples.
- Discusses and clarifies the pile-rock mass interaction.
- Introduces a complex 2D numerical model including shaft roughness, significantly contributing to understanding the pile-rock mass interaction mechanisms.

✉ Adis Skejić
askeja@live.com; adis.skejic@gf.unsa.ba

Dejan Gavrić
dejan.gavric@ipsa-institut.com

Mario Jurišić
mario.jurisic@tel.net.ba

Đani Rahimić
djani.rahimic@unmo.ba

[1] Faculty of Civil Engineering, University of Sarajevo, 71000 Sarajevo, Bosnia and Herzegovina

[2] IPSA Institute, Sarajevo, 71000 Sarajevo, Bosnia and Herzegovina

[3] Hering dd, Široki Brijeg, 88220 Široki Brijeg, Bosnia and Herzegovina

[4] Faculty of Civil Engineering, University "Džemal Bijedić" Mostar, 88000 Mostar, Bosnia and Herzegovina

**Keywords** Pile load test · Bored piles · Conglomerate rock mass · Numerical modeling

## 1 Introduction

Bored piles socketed into different rocks are often used to carry extreme structural loads. When designed to support heavy loads, these piles are usually arranged in a group, significantly influencing their behavior compared to a single pile load-settlement response. Since the testing of large-scale socketed pile groups is not rational, the data collected from isolated pile load tests are still used in designing pile foundation systems. According to Haberfield and Lochaden (2019), piles socketed in rock should be designed only to assess settlement at serviceability loads, not by shaft and base resistance estimates according to relevant standards.

Static load testing is the best solution for investigating and understanding pile load settlement behavior. Unfortunately, there is a shortage of good quality static load test data, especially for bored piles built in the conglomerate rock mass. Additionally, since conglomerate cementation can vary significantly with depth, strength, and the stiffness of foundation rock mass are essential for pile group settlement prediction. In the absence of the load test results, selecting appropriate pile diameter and length for deep foundation systems in such materials is usually made using empirical correlations to conservatively assumed uniaxial compressive intact rock strength (UCS) values. The lack of appropriate input parameters about rock mass can lead to overdesigned deep foundations and increased construction time and cost. One of the best solutions for this problem is to perform static load testing with a properly defined testing program. The testing of piles in the rock mass is rarely performed to the ultimate bearing capacity of the rock mass since structural capacity often controls the maximum load at the top of the pile (Haberfield and Lochaden 2019). Therefore, rock mass deformation modulus is needed to obtain a more accurate estimate of the peak side resistance of a socketed part of the pile (Asem and Gardoni 2019; Seidel and Collingwood 2001; Williams and Pells 1981). Since the displacements and deformations can be measured along with the test pile, numerical back analyses can be used to define the appropriate rock mass stiffness and strength parameters. Numerical modeling is widely used in static pile load test simulations to generate synthetic data on how material characteristics influence the load settlement behavior (Alnuaim et al. 2020; Eid and Bani-Hani 2012; Eid and Shehada 2013; Vu 2013). Since such modeling relies on certain assumptions in setting parameters, experimental results are often used to provide verification benchmarks. This paper describes experimental investigations of three pile load tests. It compares the results of numerical models with those obtained in the field for one of the test piles. Special attention was paid to how static load tests can be arranged to gain sufficient data to select working pile lengths appropriately. Specifically, one of the three tested piles was designed to reach the irreversible displacement range (commencement of full slip) since these load tests are precious not only for a specific project but to the entire deep foundation engineering community (Turner 2006).

### 1.1 Field Testing of Axially Loaded Piles in Rock

Pioneering works in experimental static pile load testing in rock include (Horvath et al. 1980; Pells et al. 1980; Rosenberg and Journeaux 1976; Rowe and Armitage 1984; Seychuk 1970; Thorburn 1966; Williams 1980; Williams et al. 1980), and many others. The data from those field tests were essential for formulating empirical methods used to predict the ultimate bearing capacity of socketed piles. Still, due to numerous factors influencing the load settlement response of piles, load testing is also performed in the more recent period (Alrifai 2007; Barbalić et al. 2007; Carrubba 1997; Chen et al. 2018; Ervin and Finlayson 2006; Kou et al. 2016; Omer et al. 2002; Russo 2012; Seol and Jeong 2007; Yong et al. 2017; Zlatar 2008). The main differences between large-scale static load tests reported in the literature include piles characteristics (diameter, socket length, construction technique), rock mass-pile interface roughness, and rock mass characteristics (rock type, rock mass stiffness, intact rock strength).

Socket lengths ranged from 1.37 m ((Horvath et al. 1983)-0.71 m diameter auger excavated piles in shale rock) to 11.0 m ((Carrubba 1997)-1.2 m diameter pile drill by a rock bit in gypsum rock mass).

Rock-pile shaft interface roughness prior to concrete installation was repeatedly missing information in those case study papers, although the designers are encouraged to measure socket roughness during pile construction wherever possible (Seidel and Collingwood 2001) because this factor can have a significant influence on the pile side resistance (Gutiérrez-Ch et al. 2021a; Xu et al. 2020b). The importance of side interface roughness for the pile shear resistance is interpreted by generating additional interface normal stress, induced as dilatation at rough pile-rock contact occurs. Some empirical models developed to account for side roughness on ultimate shaft resistance along with the unconfined compressive strength (Gutiérrez-Ch 2020c; Horvath et al. 1983; Kulhawy and Phoon 1993; Seidel and Collingwood 2001; Zhang and Einstein 1998) indicate the importance of this factor.

The base cleaning technique undoubtedly influences the ultimate toe resistance. Ineffective base cleaning can

lead to a gradual increase in the base resistance and, more importantly, the negligible contribution of toe resistance mobilized at the serviceability limit state. The differences in tested piles led to various values of maximum load and displacement reached during the testing. The ultimate bearing capacity responding to settlements of approximately 10% of pile diameter was not achieved even for tests with minimum socket lengths. In a total of 5 load tests described in Carrubba (1997), none of the tested piles revealed apparent failure under a maximum axial load of 10.0 MN. Even for relatively compressible rock mass (marl), a maximum settlement of only 2% of pile diameter was reached for a pile socketed 7.5 m in the rock. Similar conclusions are obtained in (Akgüner and Kirkit 2012; Kou et al. 2016; Zhan and Yin 2000). However, ultimate mobilization of pile side resistance is expected at displacement in the range of 5.0–10.0 mm (Basarkar and Dewaikar 2006; Horvath 1982), so the results from static load tests are beneficial for defining ultimate shaft resistance of socketed pile even if not performed up to maximum resistance.

Some differences in rock-socket capacities might be expected between piles built-in sedimentary and other rock types (igneous and metamorphic) (Ng et al. 2001). Although this discrepancy may be attributed to the stiffness of rock mass or pile-rock interface roughness, some specific aspects of a particular rock mass may still influence the load settlement behavior. For example, over 100 case studies were reported in Rezazadeh and Eslami (2017), and a new method was proposed for determining shaft bearing capacity for different types of rock.

Pile tests reported in the literature were built up in different rock mass types. Still, interestingly, none of the experiments was conducted on piles in conglomerate rock. Since the experimental results published in the present study includes the piles testing in a particular rock mass that is rarely reported in the literature, the reported results become more practical.

### 1.2 Small-Scale Testing of Axially Loaded Piles in Rock

Understanding pile-rock interaction mechanisms can be significantly improved by observing the load-settlement behavior and axial deformations distribution along with the socket in laboratory small-scale models. These tests were usually performed in centrifuge facilities, and the examples of such physical analyses of reduced-scale socketed piles may be found in (Dykeman and Valsangkar 1996; Gutiérrez-Ch et al. 2020a; Gutiérrez-Ch et al. 2021b; Leung and Ko 1993), among others. Small-scale testing was sometimes performed as conventional, without centrifuge (Benmokrane et al. 1994; Dai et al. 2016), noting that this approach may lead to overprediction on the ultimate unit shaft resistance as the magnitude of friction mobilized along the pile socket depends upon the confining pressure and lateral stiffness of surrounding rock (Leung and Ko 1993).

The advantages of small-scale socket models, compared to full-scale tests, were recognized by Xu et al. (2020). These authors applied advanced imaging techniques (micro X-ray computed tomography) to monitor axially loaded socket behavior, noting that this approach can not be combined with full-scale tests. The complex pile-rock interaction mechanism was described comprehensively by observing the pile base and shaft interface.

Some simplifications must be introduced during the preparation of the small-scale models. Natural rock is usually replaced by synthetic materials (for example, mixtures of sand, cement, bentonite, gypsum powder, water). Those manufactured mixtures were prepared to represent rock mass with appropriate uniaxial strength. Piles were simulated by different artificial materials like plexiglass or aluminum tubing, aiming to achieve axial stiffness of full-scale piles. The additional parameter used for scaling is related to the roughness of the shaft surface. Different authors have used various approaches to introduce the rough surface, resulting in shaft surface conditions appropriate for full-scale socket profiles shaped during drilling operations. Dai et al. (2016) used 50.0 mm piles with asperity amplitudes equal to 1.0, 2.0, and 3.0 mm, and the sinusoidal wavelength of 40.0 mm. A similar approach was used by Gutiérrez-Ch et al. (2020a) with an asperity amplitude and a wavelength of 0.8 mm and 10.0 mm, respectively. Finally, Dykeman and Valsangkar (1996) simulated rough sockets by machining circular asperities, 0.5 mm wide, 0.5 mm deep, and spaced at 5.0 mm intervals. Generally, the relative measure of roughness defined by Horvath et al. (1983) ranged from 0.0 (smooth) to 0.232 (very rough).

This paper will only use qualitative results for a relatively small settlement ratio obtained from model studies as valuable data to interpret full-scale test results. The most important finding from small-scale simulations indicates that the shaft resistance is first fully mobilized at a settlement ratio in the range of 1% to 2% for the shaft only and complete socket piles, respectively. Additionally, the ultimate shaft resistance was first mobilized in the upper portion of the pile, noting that degradation of asperities and significant bond breakage becomes more relevant for socket settlements over 3% of pile diameter (Gutiérrez-Ch et al. 2020a), which is rarely reached in the full-scale tests. When model pile sockets were constructed with a styrofoam base to exclude the base resistance, side resistance mobilized near the top and bottom of the pile is higher than side resistance in the middle part of the socket (Dai et al. 2016; Gutiérrez-Ch et al. 2021b). Regarding the roughness influence, it is repeatedly

confirmed that the asperities on the socket shafts increase the side resistance compared to smooth shafts.

### 1.3 Conglomerate Rock Mass

The geotechnical characteristics of conglomerate rock mass are challenging to define. Geotechnical parameters of this material are heavily influenced by the dimension of tested volume and the interpretation methodology followed by testing (Sousa et al. 2020). The measurements of its intact strength and stiffness properties are largely constrained by extracting representative samples that meet the recommended testing requirements (Akram et al. 2010). The tests conducted on small-scale specimens in the laboratory generally do not yield strength and deformation parameters that would directly be applied to the rock mass from which the specimens were collected (Bieniawski and Heerden 1975). Selecting appropriate specimens for laboratory testing is another challenge since the diameter of the sample should be a minimum of 10 times the largest grain (International Society for Rock Mechanics 1978). Using different correlations relating the UCS of intact rock to deformation modulus (Asem and Gardoni 2019; Rowe and Armitage 1987) becomes unreliable because of the value of uniaxial strength itself. The same problem was found during dilatometer testing of such materials (Sousa et al. 2020) due to the small tested volume that may not represent rock mass. Another option to determine the rock mass deformation modulus is plate load tests. Even when performed, this kind of testing could lead to misleading results due to the material heterogeneity if a relatively small diameter of the plate is used. Some results from the published literature indicate that the values of conglomerate deformation modulus ($E_m$) range from 641.0 MPa to 1511.0 MPa (Sousa et al. 1997).

Determining the strength parameters of the conglomerate rock mass is another difficult task. Examples of conglomerate direct shear testing in the laboratory exist (Krsmanović 1967). However, during direct shearing, the complex stress–strain response brings inconvenient interpretation if relatively simple constitutive models were used.

Since conglomerate cementation can be different even at close distance locations, a set of large intact specimens were sheared in direct shear test conditions in the present study. The obtained results were used to define the strength parameters around the socket of the test piles. These parameters will serve in numerical simulations of the one selected static pile load test, and the outcome will be compared against measurements. Additionally, the ultimate pile resistance was compared with the empirical correlation results, which rely on intact strengths determined on relatively small specimens that do not meet the recommendation given by International Society for Rock Mechanics (1978). As a result, the possibility of using these material characteristics to predict pile capacities in similar conditions is investigated.

### 1.4 Numerical Modeling of Axially Loaded Rock-Socket Piles

Numerical modeling of axially loaded piles in the rock was first introduced in the late seventies (Pells and Turner 1979). The beginning of the current century saw significant additional progress in analysis techniques using primarily finite element and finite difference methods. Developed numerical models of full-scale pile load tests may be found in works by (Eid and Bani-Hani 2012; Haberfield and Lochaden 2019; Kirkit et al. 2010; Wang et al. 2020), among others. Different assumptions were used to investigate pile geometry and rock characteristics on socket-rock interaction. These models were formulated in 2D by modeling the pile as an axisymmetric 2D elastic solid element and planar contact surface without irregular asperities. Since the pile roughness was not explicitly included in the socket shaft geometry, an interface element is usually introduced as simplification (Mahmoud and Samieh 2017; Rahman et al. 2019). Some difficulties were pointed out in case the roughness of the pile-rock interface would be modeled by a large number of irregular asperities (Kong et al. 2006), noting that it would be highly time-consuming, especially since it does not eliminate the need for rock-concrete bonding characteristics recognized as very important in numerical modeling of rock-socketed piles (Cheng et al. 1996; Zhou et al. 2020).

Nevertheless, (Hassan and O'Neill 1997) used the finite element method and explicitly included idealized sinusoidal undulations and pile-rock contact bonding in the axisymmetric 2D model. The contact between rock mass and sinusoidal wave surface was modeled with a sliding friction angle equal to 30˚ and without cohesion, aiming to stimulate the side surface conditions representative of shale rock masses. Additionally, (Melentijevic and Olalla 2014) modeled the asperities as idealized triangles. The results indicated that the influence of different roughness classes is negligible for the low load levels and generally of much lower importance than expected. A similar approach was later used by (Dai et al. 2016; Gutiérrez-Ch and Melentijevic 2016; Zuo et al. 2004), who simulated the undulations by sinusoidal profile, including the contact bonding with reduced strength at the shaft surface, similar to Hassan and O'Neill (1997).

The interface irregular surface was currently considered using idealized roughness data in distinct-element numerical simulations (Gutiérrez-Ch et al. 2019, 2020b, 2021a). These authors successfully compared DEM results with empirical formulations and developed a methodology, which based on a few laboratory tests (UCS tests and directs shear tests), can use 3D DEM numerical models as a powerful tool to simulate the load capacity and shaft resistance response of

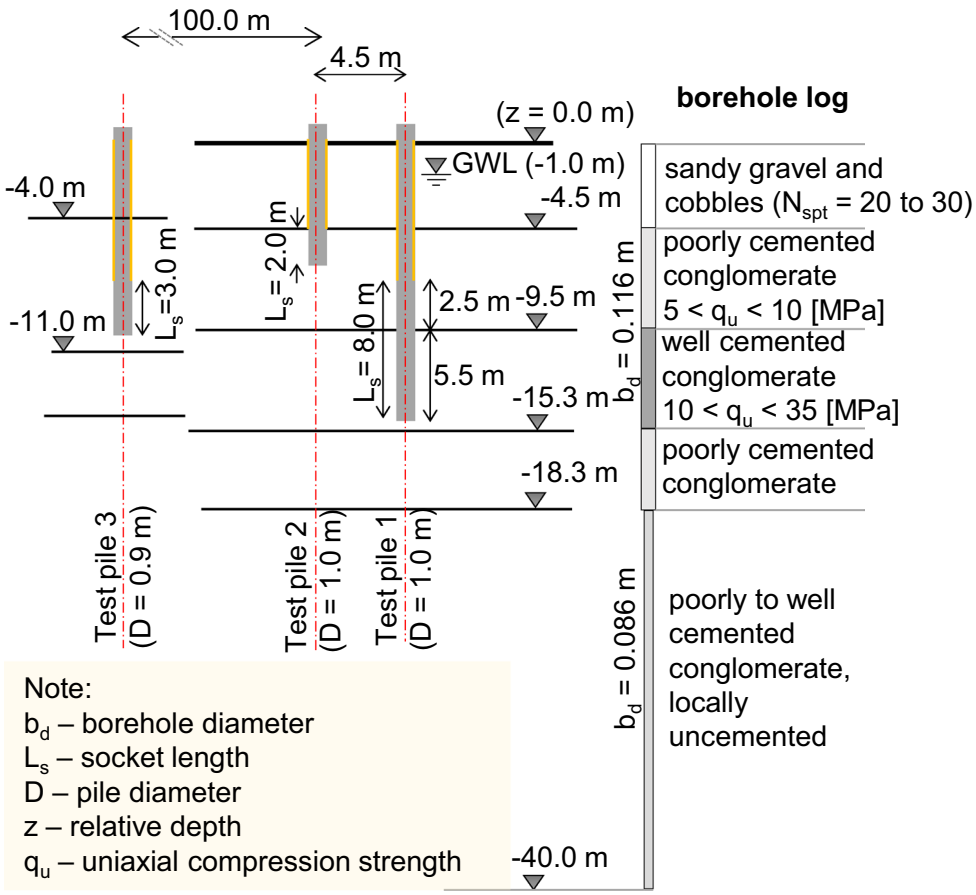


**Fig. 1** Geotechnical characterization of test pile location

rock-socketed piles considering socket roughness. These DEM results showed that roughness is an important factor that significantly increases rock-socketed piles' load capacity and stiffness.

The selection of appropriate input parameters for numerical modeling (primarily the rock characteristics and shaft surface roughness) of piles in rock rarely includes independently defined strength parameters. These parameters influence load settlement behavior significantly if the test is performed on a relatively large settlement. This approach was considered in the present study to compare numerical and experimental results. Since the pile shaft surface roughness was measured, a back numerical analysis that includes appropriate sinusoidal undulations was used to obtain representative values of pile-shaft contact strength that simulate observed pile response.

## 2 Test Piles Details

### 2.1 Geotechnical Site Characterization

Figure 1 shows the geotechnical characterization of the location and test piles socket lengths ($L_s$) and a typical borehole log at the test piles location obtained by three investigation boreholes.

The boreholes B1 and B2 were drilled next to the test piles 1 and 2, confirming the same engineering-geological conditions. The near-surface soil consists of relatively low strength and stiffness sandy gravel with cobbles down to the depth of 4.5 m ($N_{spt}$ ranges from 30 to 40). This soil does not provide the required bearing capacity and stiffness to carry an additional load from the heavy structure designed at the location. At the 4.5 m depth from the surface ($z = 0.0$ m) illustrated in Fig. 1, 5.0 m deep poorly cemented conglomerate rock was recognized by drilling rate and visual inspection of borehole core. Below this layer, a 5.8 m thick layer of the well-cemented conglomerate was encountered to a depth

**Table 1** Data related to drilling tools used for test piles

| Pile No | Depth range [m] | Drilling tool |
|---|---|---|
| TP1 | 4.5–14.0 | Core barrel + casing |
| | 14.0–15.0 | Core barrel |
| TP2 | 4.5–6.5 | Core barrel + casing |
| TP3 | 4.0–7.0 | Core barrel + casing |
| | 7.0–10.0 | Core barrel |

of 15.3 m. The poorly cemented conglomerate was observed from 15.3 to 18.0 m, and it is followed by a conglomerate with a varying degree of cementation until a borehole (B1) depth of 40.0 m was reached. The additional information gained during the borehole drilling investigation was the groundwater level measured at one meter below the ground ($z = -1.0$ m), as indicated in Fig. 1. This water level agrees with the water surface elevation in the nearby river. Similar conditions were confirmed at borehole B3, located 100.0 m from the first two investigation points (at the test pile 3-TP3) with different depths of gravel and conglomerate layers, as indicated in Fig. 1.

A comprehensive set of useful information about in situ geotechnical conditions was gained during the bored pile drilling operations, especially for the poorly cemented conglomerate that could not be sampled during the small diameter borehole drilling. Different excavation techniques (core barrels, drilling bits with buckets, heavy chisel, and grabs) were combined to construct the first working pile used as part of an investigation program. The depth of this 1.5 m diameter pile was 23.0 m. The drilling process included driving a temporary steel casing that was advanced after rock breaking and grabbing the excavated material using drilling bits, heavy chisel, and grabs. The maximum installation depth of the steel casing was 14.0 m since any further progress was disabled by rock mass friction resistance. The detailed information on drilling tools used for test piles at different depths is shown in Table 1. Collected rock samples were used to determine unconfined compressive and shear strength presented in the following two sections.

## 2.2 Unconfined Compressive Testing of Intact Specimens

The drilling operation significantly disturbed the collected rock core from investigation boreholes. The intact samples longer than 10.0 cm could only be assembled in the well-cemented conglomerate (for example, at 10.0–15.3 m depth in Borehole B1), indicating RQD value in the range of 30% (average value for 5.3 m interval). These 10.016 cm diameter samples were cut to maximum obtainable lengths ranging from 10.0 to 20.0 cm and tested in a uniaxial testing machine (a total of 13 specimens). After the correction of test results due to sample length to diameter ratio (ASTM D2938-79) was applied, UCS ranging from 10.0 to 35.0 MPa, with an average value of 19.0 MPa were confirmed. These values were consistent with the results published in Šunjić et al. (2020). However, since the results were very discrete, it will be used only as indicative, noting that the grain size and matrix condition significantly influence the UCS for this kind of material. In most tests, the specimen failure was caused by splitting along the vertical axis by forming vertical cracks that pass through the matrix (Fig. 2).

The same average unconfined compressive strength was confirmed for six specimens, 150.00 mm in diameter collected from 13.0 m depth (cut from pile core of well-cemented conglomerate) at test pile 3, located 100 m from test piles 1 and 2.

Excavated material collected by drilling bored pile (TP1 and TP2) in a poorly cemented rock mass (depths ranging from − 4.5 to − 6.5 m for TP2 and − 7.5 to − 8.5 m for TP1) was cut to a relatively small but maximum obtainable 15.0 cm in diameter and height. These specimens were tested in uniaxial compression to measure poorly cemented conglomerate strength. Observed UCS values ranged from 5.0 to 10.0 MPa with an average value of 7.5 MPa and coefficient of variation equal to 21%. These results were relatively less scattered when compared with the well-cemented conglomerate, but still, it could only be used as an indicative UCS value.

These results were compared with field estimates of the UCS of intact rock proposed by Hoek and Brown (1997).

**Fig. 2** Typical crack observed after intact specimen failure during uniaxial testing


**Fig. 3** Excavated material during pile drilling at the location: **a** Grain matrix interface failure for poorly cemented conglomerate; **b** Combined failure including grains and matrix for the well-cemented conglomerate

The crumbling in poorly cemented conglomerate during hammering of rock mass occurred on the grain-matrix interface (see Fig. 3a) rather than combined failure that includes grain collapse as observed in a well-cemented conglomerate (see Fig. 3b).

Four additional samples were collected from the TP3 borehole during the pile drilling process (depths ranging from − 7.0 to − 10.0 m, corresponding to the socket length). These samples, 10.0 cm in diameter and 12.5 cm in height, were tested for failure. Average UCS equal to 5.1 MPa was obtained, confirming similar intact strengths as measured for samples collected from the TP1 and TP2 locations.

### 2.3 Direct Shear Testing of Intact Specimens

Intact rock samples were shaped from the core collected during the test pile (TP3) socket construction (depths ranging from − 7.0 to − 10.0 m, corresponding to the socket length). A total of six pieces were shaped by a rock cutting machine and tested in shear apparatus with specimens having the dimensions 25.5 × 12.5 × 12.5 cm. The samples were tested for different normal stresses to analyze the influence of the normal stress range on strength envelope curvature. All the specimens were cut to fit the shear box leaving the 2.5 mm gap at the sample sides, and a strong self-compacting grouting mixture was used as an encapsulating compound. First, a plastic wrap was applied around the sample to prevent the penetration of encapsulation material. Then the specimen was positioned in the lower box and potted 2.0 mm below the top of the bottom half of the box. After the compound had hardened, silicon was applied to fill the 2.0 mm gap and an additional 3.0 mm above the shear plane. Finally, the upper box was placed on 1.0 mm in diameter steel wire inserted between the top and bottom box halve, forming the total gap thickness of 5.0 mm at the shear plane level. The steel surfaces were greased to reduce sliding friction. The selection of gap thickness was challenging since this dimension provides another possible source of unwanted effects. Based on the (ASTM D5607–02 2008), a gap zone of at least 5.0 mm between upper and lower encapsulating material should be free, which is less than 10.0 mm suggested by International Society for Rock Mechanics (1978). The gap between the lower and upper box in the present study was fixed to 5.0 mm since the systematic investigation of the effects of opening size with respect to shear resistance is outside the purpose of this work. The shearing apparatus is indicated in Fig. 4.

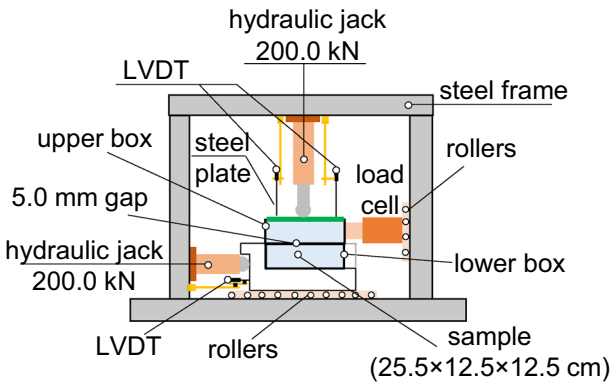


**Fig. 4** Large direct shear test set up

The lateral displacement was applied to the lower box with a constant displacement rate equal to 0.1 mm/min, while the upper box was restrained by the load cell to the fixed frame. An acquisition system connected to a personal computer continuously collected the data on the lateral displacement of the lower box and mobilized resistance at the upper box. The planar, nominal shear surface area was equal to 0.031875 $m^2$. Constant normal stress conditions (test 1: 0.125 MPa; test 2: 0.3 MPa; test 3: 0.65 MPa and test 4: 0.95 MPa) were selected for all tests to simulate the normal stress conditions around the pile. An illustration of the failure surface is shown in Fig. 5b, together with the specimen

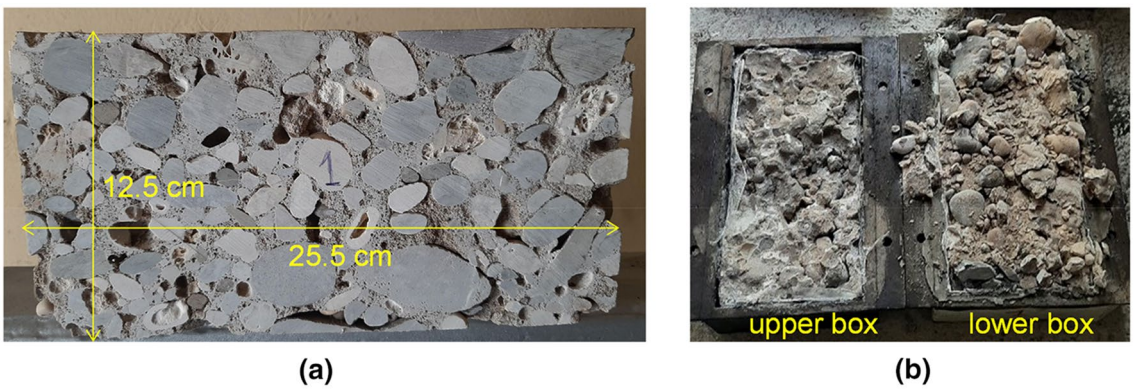


**Fig. 5** Specimen tested in the direct shear test: **a** Before testing; **b** after the failure

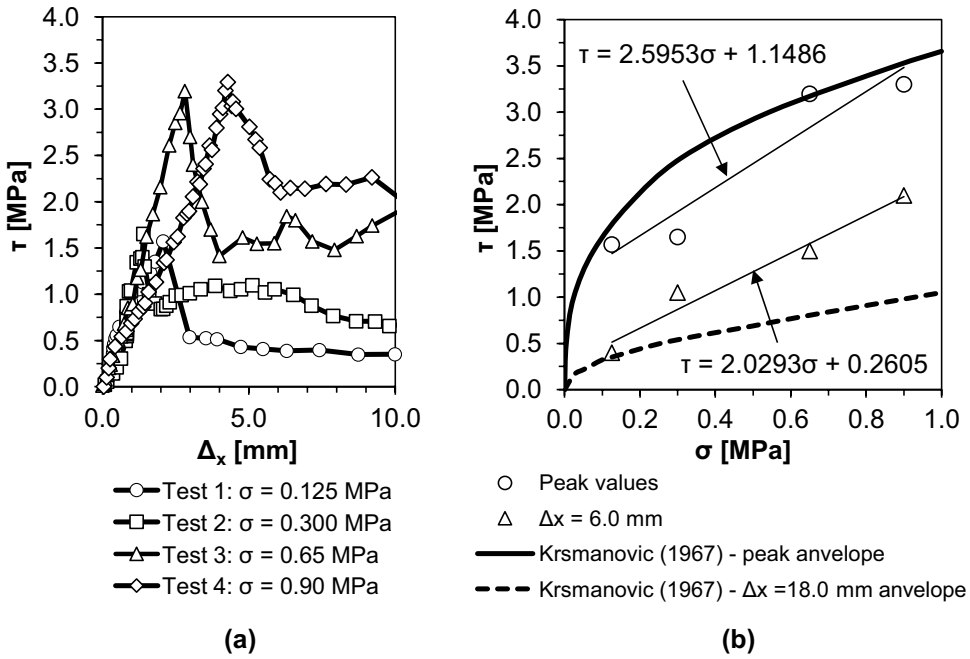


**Fig. 6** Direct shear tests results: **a** Shear stress vs. shear displacement; **b** Shear stress vs. normal stress and selection of strength parameters used in numerical simulations

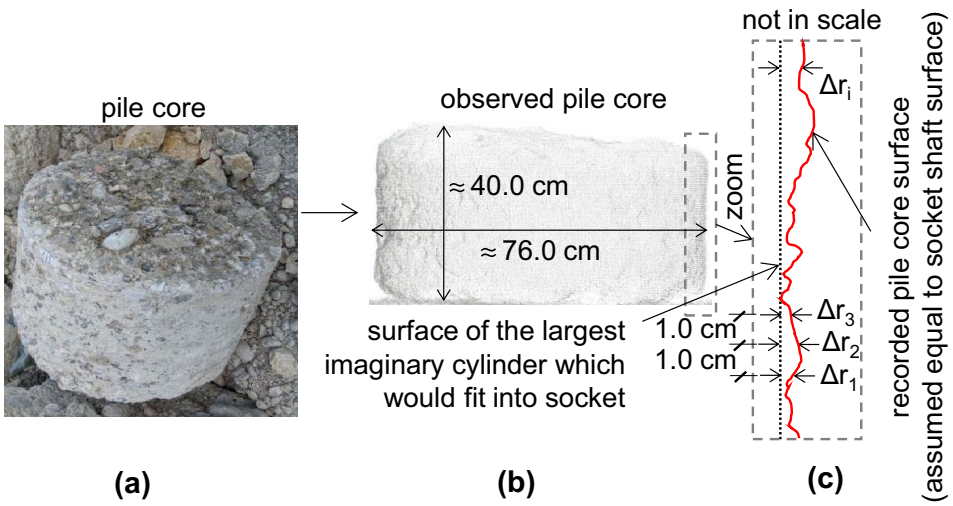


**Fig. 7** Illustration of roughness measurement: **a** Intact rock mass collected by core barrel drilling technique; **b** pile core surface recorded by laser scanning results; **c** roughness interpretation principle (Horvath et al. 1983)

condition before testing (Fig. 5a). The typical shear stress vs. horizontal displacement and normal stress vs. shear stress diagrams are shown in Fig. 6. The results of the four tests were shown because the remaining two tests deviated from the values that could have been expected. These two specimens could not be considered because the structure of the intact material was different from the other four samples (a more large-grained conglomerate was recognized after visual observation of the failure surface). Similar observations were reported in Krsmanović (1967).

An increment in shear stress at constant normal stress resulted in the fissures appearing in the vicinity of the shear surface, overcoming the internal strength of the rock. The internal failure occurred at horizontal displacement ranging from 1 to 4 mm (Fig. 6a). Since the shearing is continued at larger horizontal displacements, the mobilized shear stress decreases with increasing displacement following strain-softening behavior. Linear envelope approximation for different values of shear displacement was shown in Fig. 6b, indicating the Mohr–Coulomb effective strength parameters (c' and φ'). Aiming to compare strength parameters with the previous investigations, the peak and 18.0 mm horizontal displacement envelope were reprinted from the (Krsmanović 1967) and shown in Fig. 6b. The resulting peak shear stress from the present study matches the literature results. As expected, the mobilized shear stress at 6.0 mm horizontal

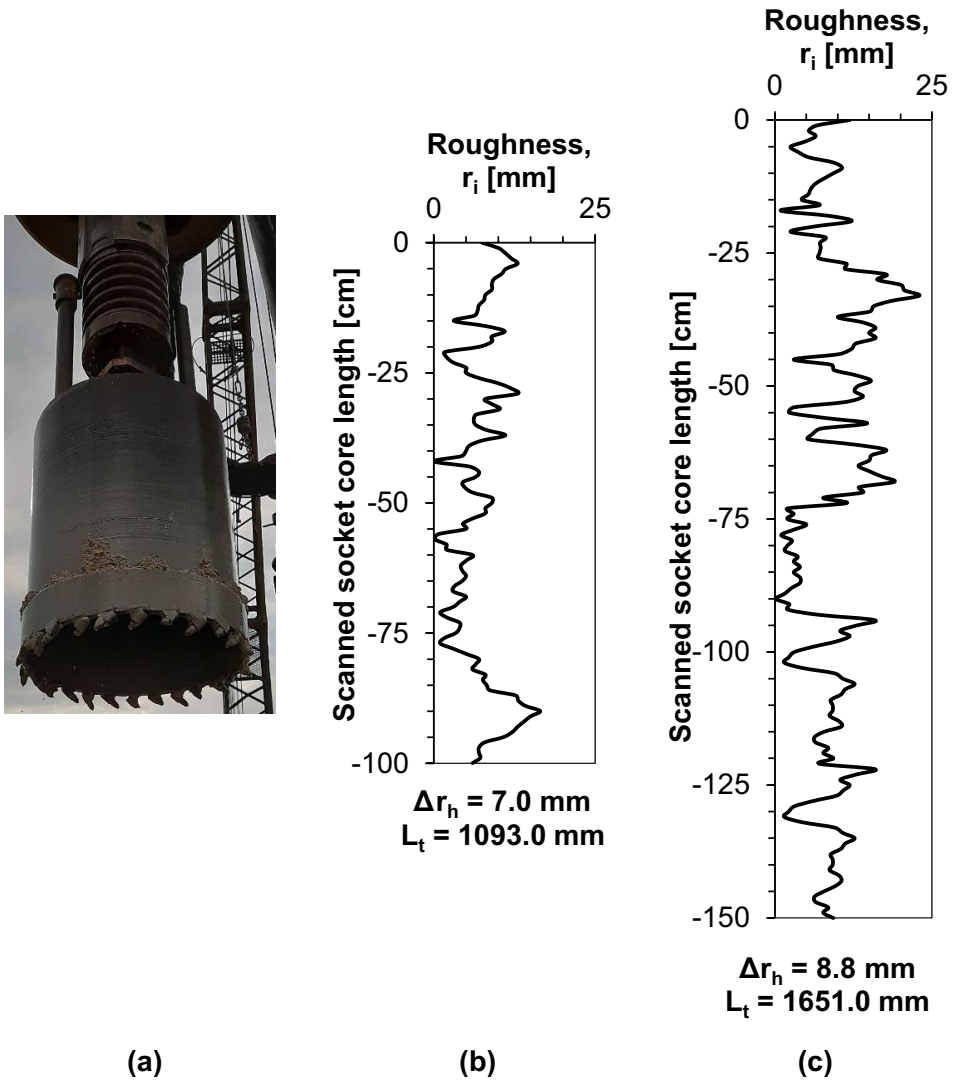


**Fig. 8** Drilling tool and measured core roughnesses: **a** Core barrel; **b** Measured roughness for TP2 and **c** Measured roughness for TP3

displacement is enclosed by the highly stress-dependent peak and residual envelopes. The selection of appropriate rock mass parameters for numerical simulation will be described in the numerical modeling section of this paper.

## 2.4 Socket Sidewall Roughness

Rock material collected from the core barrel during pile construction (see Fig. 7a) was scanned using a laser-based profiling technique to obtain the roughness of the shaft.

Trimble TX5 laser scanner with 2.0 mm standard deviation accuracy was arranged next to drilled core samples, and 3D point clouds of pile surface were recorded. The core segments collected from the socket length of TP2 and TP3 were recorded, and the different patterns of irregularity were recognized along the core surface (Fig. 7b). The scanning results were shown in Fig. 8b, c for typical cross-sections of TP3 (150.0 cm in length) and TP2 (100.0 cm in length), which were considered representative. This pile-rock roughness profile was obtained assuming that this surface was comparable to the pile-shaft interface surface.

**Table 2** Data related to socket roughness

| Pile No | Representative profile measurements [mm] | | Field measurements [mm] | | $RF = \frac{\Delta r_h}{r_s}\frac{L_t}{L_{s1}}$ (Horvath et al. 1983) |
|---|---|---|---|---|---|
| | $\Delta r_h$ | $L_t$ | $r_s$ | $L_{s1}$ | |
| TP2 | 7.0 | 1093.0 | 500.0 | 1000.0 | 0.015 |
| TP3 | 8.8 | 1651.0 | 450.0 | 1500.0 | 0.0215 |

This assumption may be less appropriate for the 2.0 m long socket of test pile 2 since it was constructed with a casing, different from test pile 3, whose socket was drilled only by the core barrel. Qualitatively, the pile side roughness was classified as class R3 according to Pells et al. (1980) since grooves of depth and width greater than 4.0 mm, at spacing 50.0–200 mm, were visually recognized on the pile core surface (see Fig. 7a). A relatively rough borehole shaft was expected for this type of rock material, especially since the construction technique included the core barrel drilling (Fig. 8a), noting that the conglomerate side surface after drilling is affected by the matrix-grain interface strength.

Since this approach was found subjective, a more detailed interpretation of rock-socket roughness was performed by applying Horvath's solution (Horvath et al. 1983) for socket roughness defined by the factor (RF) following the interpretation given in Fig. 7c:

$$RF = \frac{\Delta r_h}{r_s} \frac{L_t}{L_{s1}} \quad (1)$$

where: $\Delta r_h$—mean roughness height (determined on the half of the socket length, $L_{s1}$), $r_s$—nominal socket radius (defined as the largest imaginary cylinder which would fit into the socket assumed equal to 0.5 m for TP1 and TP2, and 0.45 m for TP3), $L_t$—total travel length measured by laser-based profiling technique, $L_{s1}$—nominal socket vertical length associated with the estimated traversed distance.

The resulting data used to obtain the roughness factor (RF) are given in Table 2. The average roughness heights correspond to the values representative of the standard drilling tool without artificial roughening (Gutiérrez-Ch et al. 2020b), and the relatively low RF values result from a large pile radius.

It is worth noting that the recorded roughness profile is very heterogeneous and that the authors selected the representative roughness as the most appropriate. Since those values do not apply to every cross-section (slice) drawn at the recorded segment surface, it may still be considered subjective. However, the maximum height of asperities ($\Delta r_i$ as defined in Fig. 7c) was rarely higher than 2.0 cm.

## 2.5 Properties of Pile Load Tests

A total of 3 piles named test pile 1 (TP1), test pile 2 (TP2), and test pile 3 (TP3) were tested at the location to investigate the shaft and base resistance and the influence of socket length and conglomerate rock mass conditions on pile load settlement behavior. The pile load test set up is shown in Fig. 9a, with the test layout illustrated in Fig. 9b.

A relatively large distance between test and reaction piles (approximately five test pile diameters) eliminates the interaction of test pile and reaction piles in the static load test. The detailed configuration and instrumentation of test piles are given in Fig. 10, showing the total pile lengths of 15.0 m, 6.5 m, and 10.0 m for TP1, TP2, and TP3, respectively. For two reasons, the upper part of the piles was secured by a steel sleeve (thickness of 2.0 mm and outside diameter 0.82 m). First, for TP1, the sleeve simulates the conditions appropriate for working piles (piles were constructed near the river flow). Second, TP2 and TP3 sleeves were erected to exclude the contribution of the material above the socket to shaft resistance. The sleeves lengths were indicated in Fig. 10 for TP1, TP2, and TP3, respectively. TP1 was constructed in poorly and well-cemented conglomerate rock mass, with a total socket length equal to 8.0 m (2.5 m in poorly cemented and 5.5 m in well-cemented conglomerate). The base of the TP1 was formed just above the poorly cemented rock mass.

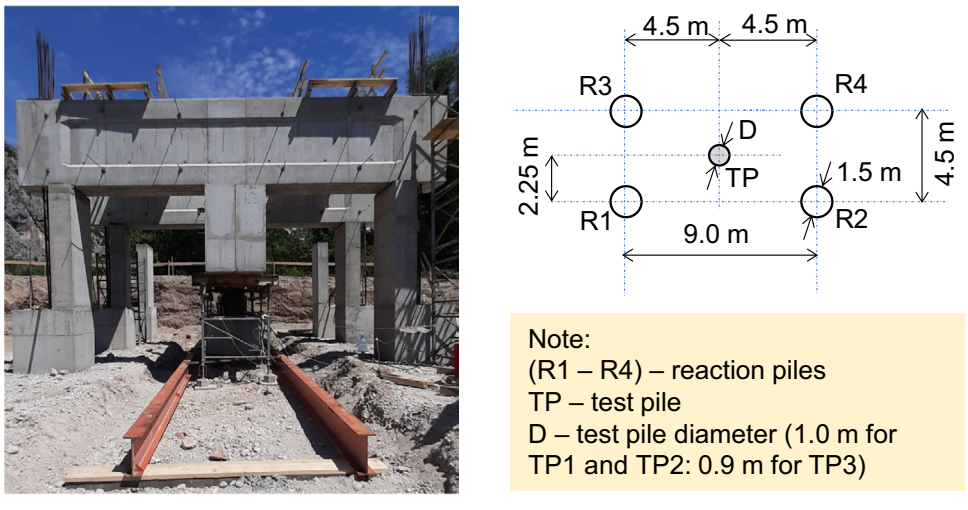


**Fig. 9** Pile load test set up **a** Photograph of test setup; **b** Test and reaction piles layout

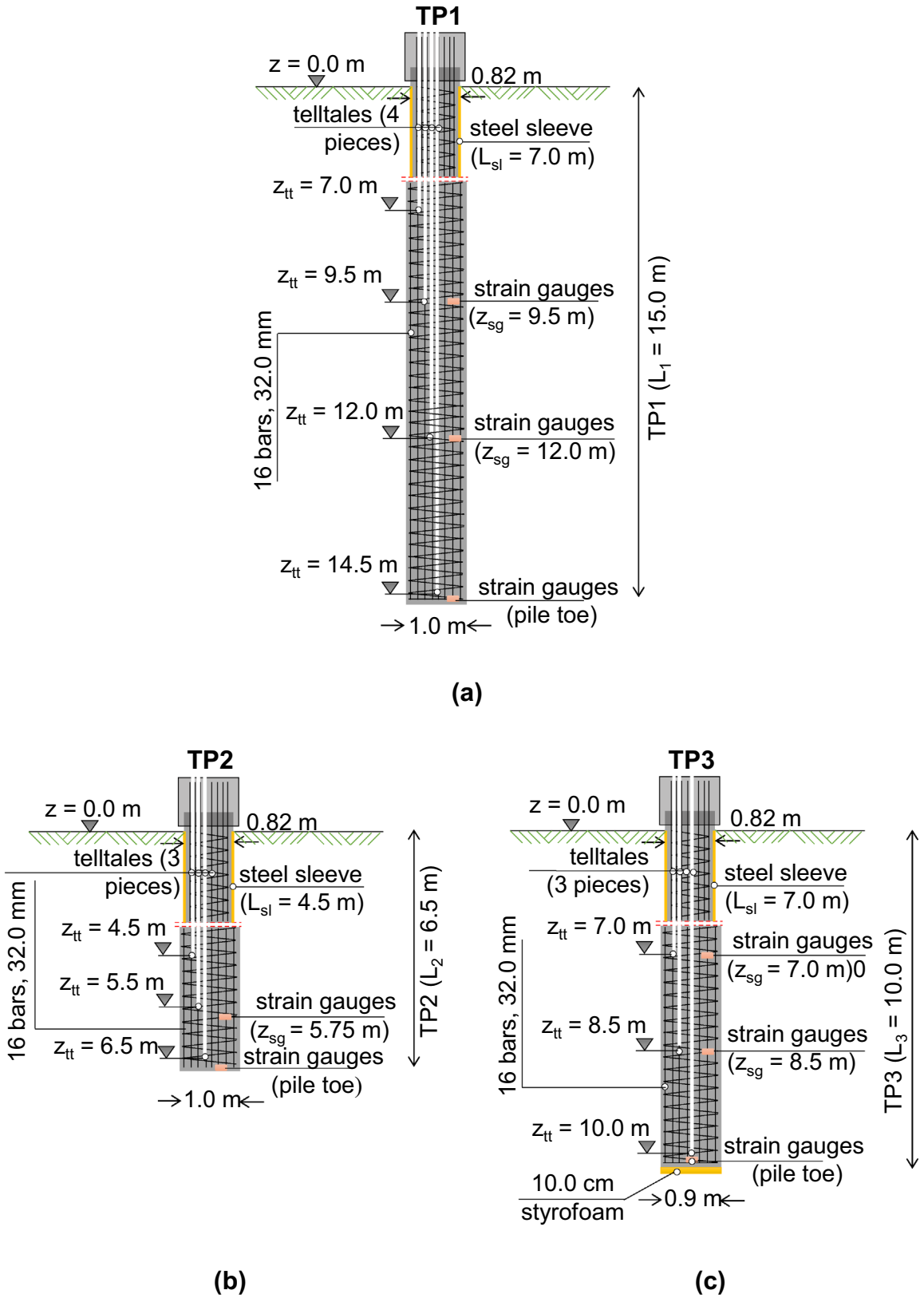


**Fig. 10** Details of a static pile load test: **a** Test pile 1; **b** Test pile 2; **c** Test pile 3

TP2 was socketed 2.0 m in a poorly cemented conglomerate, while the well-cemented conglomerate rock mass does not influence its behavior. Finally, TP3 was socketed 3.0 m in the poorly cemented conglomerate, but its toe resistance was eliminated by 10.0 cm thick styrofoam fixed to the reinforcement cage before installation. The pile diameter was equal to 100.0 cm for TP1 and TP2 and 90.0 cm for TP3. Different diameter on TP3 was the outcome of the drilling technique used in this location (see Table 1).

All the test piles were reinforced by 16 bars of 32.0 mm in diameter. The steel sleeves ($L_{sl}$ = 7.0 m for TP1, $L_{sl}$ = 4.5 m for TP2, and $L_{sl}$ = 7.0 m for TP3) were welded to the reinforcement. At the same time, the measuring equipment was mechanically connected along the steel bars before lowering the reinforcement cage to the pile borehole. Aiming to measure relative vertical displacements along with the piles (pile contraction) at selected lengths, steel telltale rods (12.0 mm in diameter) fixed at the bottom of steel guide pipes and strain gauges were tight at the specified location along with the piles. Telltales were installed at different depths ($z_{tt}$) along with the piles. As suggested in Fellenius (2017), a telltale attached to pile toe should be preferred for each test pile as a valuable addition to the static load testing program. Contraction of pile generates guide pipes shortening but leaving the rod length unaffected. The measurement of relative displacement between the pile cap and telltale rod was continuously recorded by LVDTs fixed to the top of the pile. The exact location of telltales is shown in Fig. 10 for test piles TP1, TP2, and TP3, respectively. A total of 4 telltales were installed along the TP1 and three telltales with the same characteristics along with the piles TP2 and TP3. The absolute movement of the pile toe is obtained as the measured pile shortening is subtracted from the movement of the pile head. The strain gauges installed in test piles were also indicated in Fig. 10 for three test piles. One set of strain gauges was repeatedly located at the pile base to follow the pile of base resistance mobilization during testing. Four strain gauges were located at one depth ($z_{sg}$), making it a total of 12 deformation indicators for three depths ($z_2$ and $z_3$) on TP1, two measuring points on TP2, and three measuring locations along with the socket of TP3.

After constructing the reaction and test piles, the integrity test was completed before static load testing. The piles were identified as homogenous, and the pile base-rock interface was clearly recognized. Later, the preparation work for installing the reaction system was initiated. The reaction system is shown in Fig. 11.

It consisted of four 1.5 m diameter piles and the prestressed beams anchored to the piles. First, the reaction piles were extended to the appropriate level (4.0 m above the working platform), and the pile cap was shaped at the top of the test piles. Afterwards, the reaction beams were arranged and stacked to reaction piles by prestressed steel strands (a total of four six-strand cables per reaction pile). A prestressed force equal to 5.0 MN per reaction pile was imposed to apply a vertical force that balances the capacity of 20.0 MN of hydraulic jacks. Since the reaction piles were planned to use as working piles, special attention was given to observing the reaction system. The uplift of working reaction piles was continuously measured with an accuracy of 0.1 mm to confirm that their movement is less than half of their specified permissible settlement at working load, as suggested by ICE Specification for Piling and Embedded Retaining Walls (2016).

After the reaction system and test piles had been constructed, two load cells and hydraulic jacks powered by an electric and hand-operated pump were placed on the top of the pile cap. An additional load is applied in increments according to the maintained load test defined by ASTM International (2013). Load cells used for load monitoring were calibrated before testing and supplemented by a set of strain gauges that control pile cap force value recorded by the acquisition system during in situ testing. The maximum load corresponding to $F$ = 14.8–15.0 MN was defined according to the structural pile capacity (concrete-steel coupled cross-section at the upper part of the pile). The tests were terminated once the maximum load had been reached. The piles were then carefully unloaded, and the irreversible vertical displacements were recorded.

The pile cap displacements (w) were continuously measured using HBM digital transducers (LVDT) fixed on a reference beam (steel profile HEB 300, 14.5 m in length) and controlled by surveying. The measuring range of inductive standard displacement transducers was 50.0 mm with 0.01 mm accuracy.

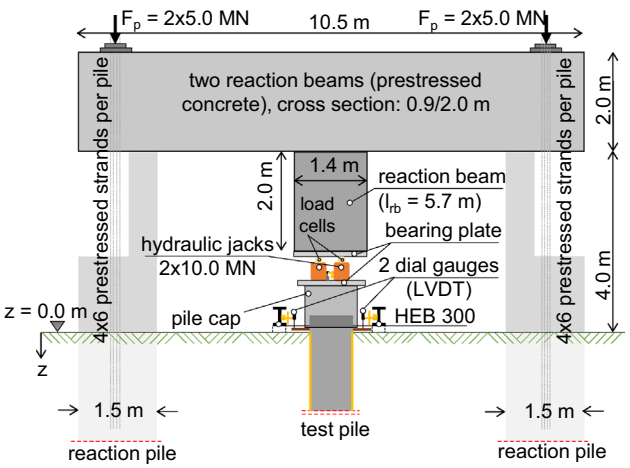


**Fig. 11** Reaction system configuration

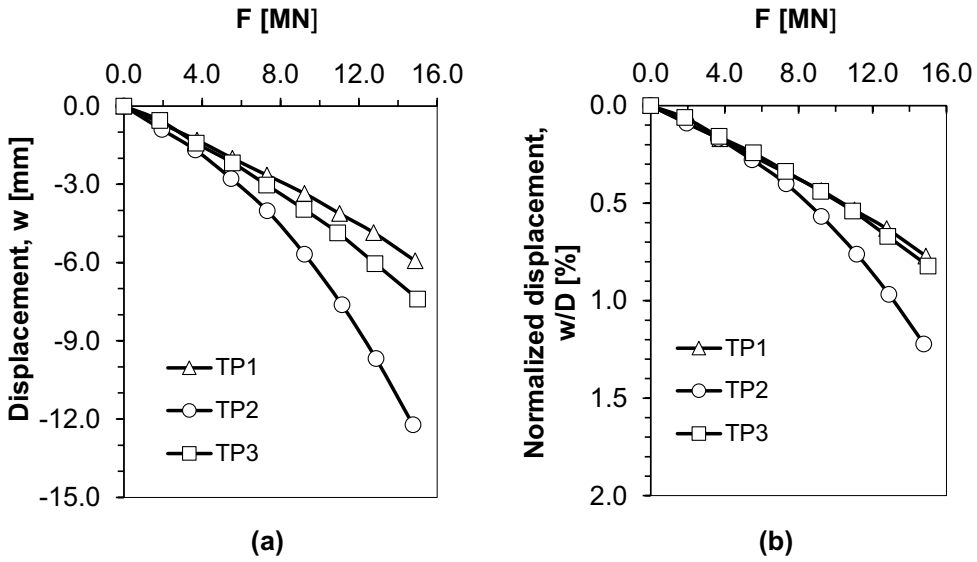


**Fig. 12** Testing results for three test piles: **a** Load vs. displacement curves; **b** Load vs. normalized pile displacement curves

## 3 Test Results and Interpretation

The test results are described and interpreted in three groups. The first group relates to conventional displacement transducer measurements at the bottom of the pile cap. The second part describes the strain gauges and the telltales measurements, while the third part includes interpretations of shaft resistance response.

### 3.1 Displacement Transducer Measurements of Test Piles Cap

Typical curves for the load (F) vs. pile head absolute (w) and relative (w/D) vertical displacement for the three test piles were shown in Fig. 12a, b.

The results obtained by displacement transducers were plotted, noting that similar results were confirmed by surveying. The ultimate rock bearing capacity could not be reached for all three test piles, not even for the TP2 with relatively short socket length in poorly cemented conglomerate rock and for TP3, which is a shear socket only. Nearly elastic

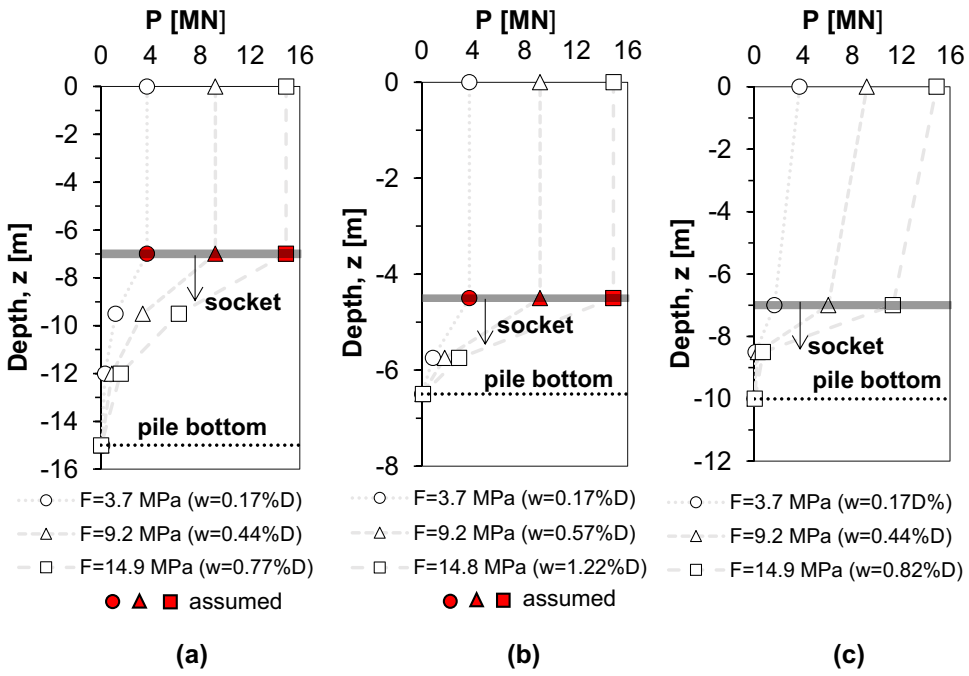


**Fig. 13** Axial load distribution in piles for different surcharge loads: **a** TP1; **b** TP2; **c** TP3

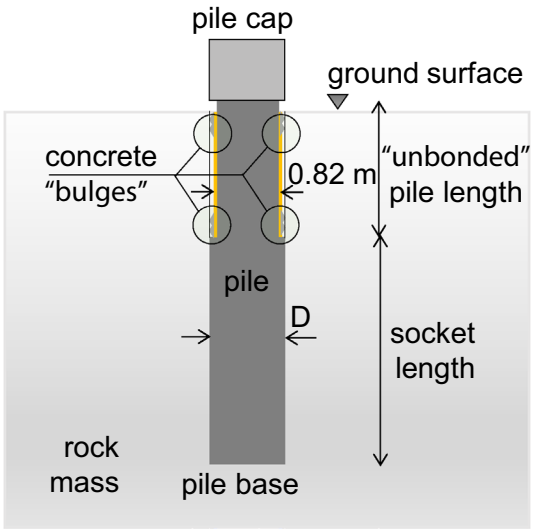


**Fig. 14** Illustration of the local bond (concrete bulges) along the sleeved pile length

behavior for the maximum applied load was observed for TP1 and TP3 piles. This may be explained by the significant ultimate side friction capacity not being reached at maximum applied force. The bottom of the pile cap of TP1 and TP3 settled 5.9 mm and 7.4 mm, respectively. The permanent displacement recorded at the end of the unloading stages (less than 1.0 mm for both piles) indicated practically elastic behavior of these two piles. The maximum recorded TP2 pile head settlements were 12.2 mm, with an irreversible displacement equal to 5.7 mm. A relatively large settlement measured after reloading indicates that some plastic slippage occurred at the pile shaft interface, making this test more valuable for interpretation, numerical simulations, and generally, for deriving practical conclusions.

### 3.2 Strain Gauges and Telltales Measurements

The axial forces distribution along with piles and pile base load were obtained using HBM linear strain gauge measurements at different levels. When using strain gauges signals for axial load distribution, the following equation was used:

$$P = \varepsilon A_p E_p \tag{2}$$

where P is axial force, ε is axial strain defined in correlation to the signals collected at the data acquisition system, $A_p$ is the cross-section area of the pile, and $E_p$ is the modulus of elasticity of the concrete pile.

The distributions of axial load along the pile at several load increments are shown in Fig. 13. Except for the TP3, strains were not measured at the top of the socket length. These strains were assumed to be the same as the pile caps' since the sleeve was installed to create a 9.0 cm gap, making it a theoretically unbonded part of the pile above the socket. This conclusion may be uncertain because the measurement at TP3 indicated some axial force reduction along the theoretically unbonded pile length, which can be explained by locally bonded parts created during the tremie pipe concrete installation (see Fig. 14). The reported results support observations from other full-scale (Chen et al. 2018; Zlatar 2008) and centrifuge tests for lower pile settlements (Gutiérrez-Ch et al. 2021b). Specifically, the mobilized axial load decreases with depth for a particular settlement. Additionally, the mobilized axial force along the pile increases as the applied pile cap load increases. The sudden reduction of strains measured along the socket indicates relatively high

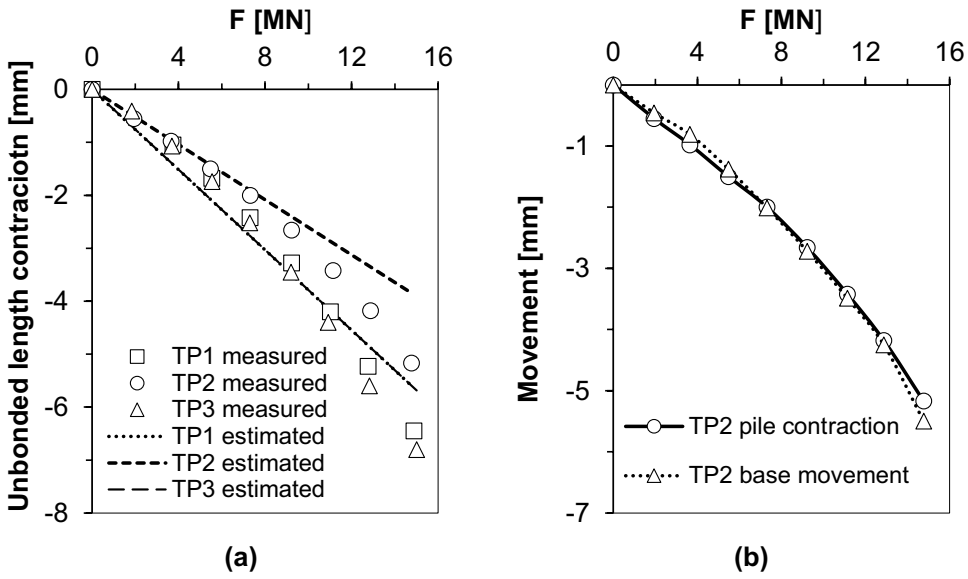


**Fig. 15** **a** Measured piles compression along the sleeved length and estimated elastic compression versus applied load (F) for 3 test piles; **b** Pile base movement ($w_b$) and pile compression of sleeved length vs. applied load for TP2

skin friction mobilized in the upper part of the socket for all the tested piles.

The pile head displacement consists of pile compression and pile socket movement. The pile compression is mainly elastic, as shown in Fig. 15a, representing the pile cap load vs. shortening of the sleeved (unbonded) part of the pile.

Those values were obtained as the difference between pile head displacements and telltales installed at the bottom of the sleeved pile lengths. Almost equal pile compression was obtained for TP1 and TP3 since these two piles had the same sleeve lengths, while approximately 30% lower values of pile compression were measured along the unbonded segment of TP2 due to shorter sleeve length. These measurements were compared to calculated elastic compression of all three test piles using the constant value of elastic modulus equal to 34 GPa, obtained according to the principle defined in a later section. The comparison of calculated and measured results indicates some discrepancies related to the influence of pile head rotation, resulting in measured pile compression larger than the theoretical one since the telltales were not located in the center of the pile, while two hydraulic jacks applied the load. Additionally, the stress dependency of concrete elastic modulus can influence the additional curvature of the load-compression curve. Nevertheless, it is generally evident that the calculated elastic compression agrees well with the measured pile shortening.

The pile socket settlements were extracted from the telltale observations. Some difficulties were recognized during the definition of pile socket settlements since pile head displacements were collected at the bottom of the pile cap, while telltales were led to the top of the cap. The relative difference between those measurement levels was 1.0 m. Consequently, the telltale reading was reduced by elastic shortening of pile cap computed by using constant pile head stiffness (k) according to:

$$\Delta h = F/k \tag{3}$$

where: $k = E_p A/h$—axial pile head stiffness, $E_p$—the Young modulus of the concrete pile (assumed constant); A—the pile cap cross-section area (1.0 $m^2$) and h—the distance between telltale and pile cap reading levels (1.0 m).

Telltale measurements from the TP1 (4 locations) and TP3 (3 locations) show negligible settlements along the total socket length. These settlements extracted from the pile cap and telltales measurements indicate less than 1.5 mm values for these two pile tests. There was little or no plastic deformation at the pile-rock mass interface, even for the maximum applied load of 14.8 MN. Such a small deformation has no reference value for analyzing pile-rock ultimate friction characteristics since it needs a certain relative displacement. However, it indicates the observed skin friction at the maximum test load. The telltale measurements for TP2 illustrated in Fig. 15b show a significant settlement of total socket length, including the pile base. Interestingly, the signals from strain gauges in TP2 were unexpectedly low compared to those settlements. The deformation equals 97.1 μm/m resulting in a 3.0 MN axial force recorded in the middle of the socket length for the maximum pile cap load of 14.8 MN. The recorded pile base load was practically negligible compared to the measured pile base settlement equal to 5.0 mm. These results can be explained in two scenarios. The first is that the strain gauge reading was not working correctly, while the second is that the pile base was not appropriately cleaned, so its resistance mobilization was minor for the range of measured settlements. Numerical modeling presented in Sect. 4 of this paper analyses

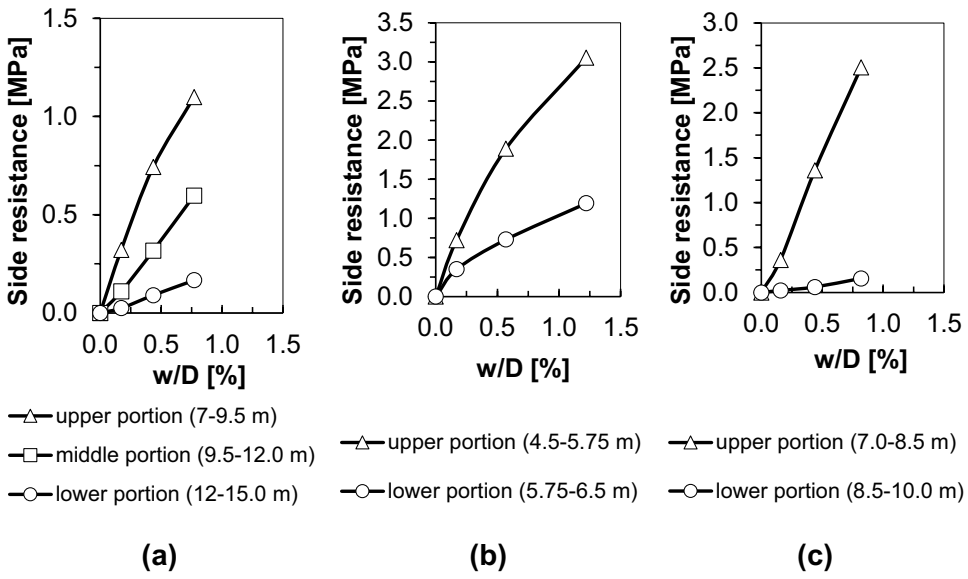


**Fig. 16** Mobilization of local side resistance for: **a** TP1; **b** TP2; **c** TP3

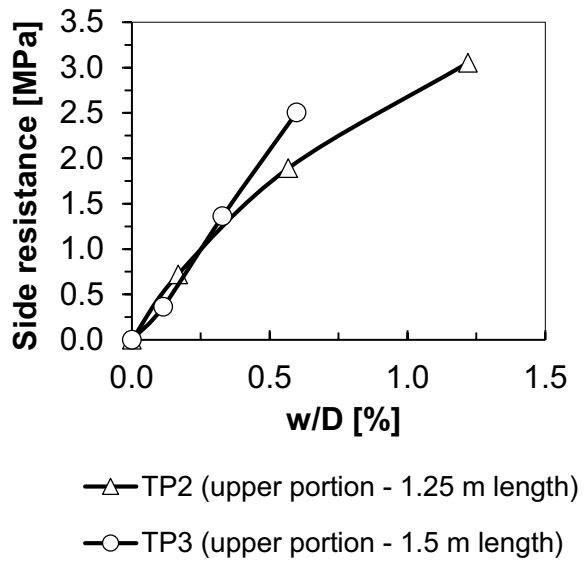


**Fig. 17** Mobilization of shaft resistance in the upper part of TP2 and TP3

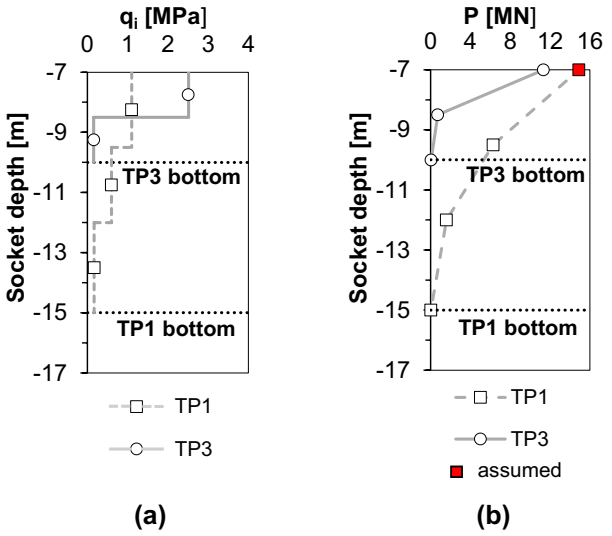


**Fig. 18** Influence of socket length (TP1 and TP3) on **a** Shaft resistance mobilization; **b** axial force distribution along with the socket

both cases to improve the understanding of pile resistance mobilization.

### 3.3 Shaft Resistance Response

The data collected by strain gauges were used further to discuss the side resistance mobilization during pile load tests. The shaft resistance was calculated from the axial force (P) distribution and corresponding pile stiffness. It is assumed that the load is distributed uniformly along the pile shaft between nearby strain gauges, and the average side resistance was determined as:

$$q_{\mathrm{i}} = \left(P_{\mathrm{i}} - P_{\mathrm{i-1}}\right)/D\pi h_{\mathrm{i}} \tag{4}$$

where $q_i$ is the average side resistance of layer $i$, $P_i$ and $P_{i-1}$ are axial forces at the top and the bottom of layer $i$; $h_i$ is the thickness of layer $i$, and D is the test pile diameter. The average side resistances for the particular segments of socket length are shown in Fig. 16.

The results were plotted against normalized head displacements, w/D. It is repeatedly measured that shaft resistance mobilization is much higher in the upper portion of the pile when compared to mobilized resistance in the lower part of the pile for each load level. These results agree with observations from small-scale models as described in the introduction of the paper (Dai et al. 2016; Gutiérrez-Ch et al. 2020a). Additionally, the mobilized shaft resistance in the upper part of TP2 and TP3 was compared in Fig. 17, noting that the settlement values for TP3 were reduced by elastic shortening measured for 2.5 m of unbonded length due to the difference in the sleeved section between these two piles.

The results indicate practically the same response for the achieved relative displacements in the range of 0.4%D. Later, for the relative pile settlements in the range of 0.4%D to 0.8%D, a notable decrease in the side resistance increment was recognized for TP2 with a shorter socket length. These results demonstrate that the side resistance in the upper part of the 2.0 m long socket reached the ultimate state after 0.8%D relative displacement. This complies with the considerable irreversible displacements measured for TP2 after reloading.

Aiming to interpret the influence of socket length on axial force and shaft resistance mobilization, a comparison between TP1 and TP3 was illustrated in Fig. 18. The sleeved lengths of these two piles were equal, while the difference in measured pile cap settlement (1.5 mm) for maximum applied load can be attributed to the socket length discrepancy. Minor socket-rock relative displacement typical tor TP1 resulted in insignificant side shaft mobilization spread along with the upper 3/4 of 8.0 long socket. Unlike TP1, noticeable shear stress was mobilized, especially in the upper half of the 3.0 m long socket making the distribution of mobilized side resistance less homogeneous for reduced socket length. The observations mentioned above indicate the influence of socket depth on relative pile-rock displacements. Namely, an increase in rock-socketed depth decreased the pile-rock relative displacement, and consequently, the pile side friction gradually decreased (Fig. 18a). Consequently, the transfer rate of the axial force from the pile to the surrounding rock decreased (Fig. 18b).

This phenomenon can be interpreted by an analytical solution of axially loaded piles in an elastic medium (for example, Wood 2003). For the same rock mass conditions and equal concrete pile Young's modulus, change in socket length will result in different axial load distribution in the socket, making it more homogenous for deeper embedded piles. A similar trend was confirmed by FEM simulations reported in Wang et al. (2020).

### 3.4 Comparisons with Empirical Relations

Experimentally measured values of mobilized shaft resistance will now be compared with the empirically determined ultimate side resistance values. It is well known that maximum shaft resistance can be estimated using the representative value of unconfined compressive strength of intact specimens. Many researchers reported different values of empirical coefficients relating UCS to the ultimate shear resistance of the socket. Most of these equations can be defined as:

$$q_{i,max} = \alpha(q_u)^{\beta}[MPa] \quad (5)$$

where $q_u$ is the UCS of intact rock, and α and β are empirical coefficients that incorporate other factors that control the side resistance (for example, construction method, type of rock, rock mass stiffness, shaft roughness). Generally, the α value ranges from 0.15 to 1.11, while β usually takes a unit or 0.5 value. The pile side roughness (data available for two tested piles, TP2 and TP3) is a key factor affecting the socket shaft resistance (Gutiérrez-Ch et al. 2021a). Consequently, the methods including roughness data as an input parameter (Gutiérrez-Ch 2020c; Horvath et al. 1983; Kaderabek and Reynolds 1981; Rosenberg and Journeaux 1976; Seidel and Collingwood 2001; Zhang and Einstein 1998) are primarily considered representative for comparison with measurements.

Some uncertainties were pointed out in Dai et al. (2016) regarding the selection of shear stress value when the back analysis is performed. Namely, since the shear stress is not constant along with the socket, different assumptions were usually introduced to determine the $q_{i,\,max}$ as defined in Eq. 5. The average value appears to be the best option for validating predictive methods (Dai et al. 2016). The present study load test's precise cast-in-place side resistance capacities are unknown since none of the piles reached failure load. Only the TP2 data may provide empirical methods validation since the other two test piles were far from the ultimate loading stage, especially TP1 with an extremely long socket for the rock mass conditions. However, the data measured for TP3 will also be shown to illustrate mobilized maximum and average side resistance at the ultimate load level during the experiment. An additional problem with side resistance prediction is the selection of representative values for UCS. Laboratory test results ranged from $q_{u,\,min} = 5.0$ MPa to $q_{u,\,max} = 10.0$ MPa, with an average value of $q_u = 7.5$ MPa, and the coefficient of variation equals 21%, which is quite scattered. However, minimum, maximum, and average measured intact strength values were used to compare the empirically estimated side resistances with average

**Table 3** Comparison of observed and estimated side resistance $q_{i,\,max}$ (MPa) for TP2 and TP3 installed in a poorly cemented conglomerate rock mass

| Test pile | TP2 | | | TP3 | | |
|---|---|---|---|---|---|---|
| RF (Horvath, (Horvath et al. 1983)) | 0.015 | | | 0.0215 | | |
| Mean roughness height, $\Delta r_h$ (Horvath, (Horvath et al. 1983)) | 7.0 | | | 8.8 | | |
| Observed maximum | 3.05 | | | 2.51 | | |
| Observed average | 2.38 | | | 1.6 | | |
| UCS [MPa] | $q_{u,\,min}$ | $q_{u,\,max}$ | $q_{u,\,ave}$ | $q_{u,\,min}$ | $q_{u,\,max}$ | $q_{u,\,ave}$ |
| SRC (Seidel and Collingwood 2001)[a] | 1.68 | 0.84 | 1.12 | 2.34 | 1.17 | 1.56 |
| Seidel and Collingwood (2001)[b], $q_{i,max} = q_u\,\alpha_q$ | 1.525 | 2.25 | 1.8 | – | 2.6 | 2.2 |
| Rosenberg and Journeaux (1976)[c], $q_{i,max} = 1.11 q_u^{0.51}$ | 2.522 | 3.592 | 3.102 | 2.522 | 3.592 | 3.102 |
| Zhang and Einstein (1998)[d], $q_{i,max} = 0.4 q_u^{0.5}$ | 0.894 | 1.095 | 1.265 | 0.894 | 1.095 | 1.265 |
| Kaderabek and Reynolds (1981), $q_{i,max} = 0.3 q_u$ | 1.5 | 3.0 | 2.25 | 1.5 | 3.0 | 2.25 |
| Horvath et al. (1983), $q_{i,max} = 0.8 q_u (RF)^{0.45}$ | 0.605 | 1.21 | 0.907 | 0.711 | 1.421 | 1.066 |
| Gutiérrez-Ch (2020c)[e], $q_{i,1\%D} = \alpha_{RF,\,0.01D} (q_u)^{0.5}$ | 0.168 | 0.949 | 0.205 | 0.4 | 2.27 | 0.491 |

[a]Best practice construction, $\Delta r_h$—Horvath's (Horvath et al. 1983) mean roughness, $E_m = 1.5$ GPa, $\nu = 0.25$

[b]$\alpha_q$ is the adhesion factor related to SRC (Seidel and Collingwood 2001). For SRC > 2.1 it is not possible to obtain the adhesion factor

[c]Equation reported in (Gutiérrez-Ch et al. 2020b) for rough piles

[d]Roughness class R3

[e]$\alpha_{RF,\,0.01D} = 10RF(L_s/D)$ for $q_u \geq 10.0$ MPa, $\alpha_{RF,\,0.01D} = 2.5RF(L_s/D)$ for $q_u < 10.0$ MPa

and maximum shear stresses from experiments. The results are given in Table 3, showing that some estimated values were very close to measurements.

The closest estimate was obtained using Kaderabek and Reynolds (Kaderabek and Reynolds 1981) and Seidel and Collingwood (Seidel and Collingwood 2001) methods. At the same time, some methods deviated significantly, noting that the average measured ultimate side resistance for TP2 is generally higher than predicted. This discrepancy may be attributed to UCS values that may be unrepresentative due to sample characteristics (relatively small specimens). The only method that resulted in overpredicted shaft resistance was Rosenberg and Journeaux (Rosenberg and Journeaux 1976). This is probably due to the approximate estimation of roughness in this method, defined as "rough piles" that may not be in accordance with the measured average roughness height. The methods of Zhang and Einstein (Zhang and Einstein 1998) and Horvath et al. (Horvath et al. 1983) notably underpredict the maximum shaft resistance. A similar trend was obtained by the Gutiérrez-Ch (2020c) method that considers a pile settlement of 1% of the pile diameter ($q_{i,1\%D}$), the socket roughness (using the Horvath's RF factor (Horvath et al. 1983)), the length of the socket ($L_s$), the pile diameter (D), and the UCS of the weaker material ($q_u$). This method, however, provides a good average shaft resistance estimate for a longer pile (TP3) with a higher RF value and for a maximum measured UCS of $q_u = 10.0$ MPa. Some deviations were also recognized between measured maximum skin friction for TP2 and TP3. This can be interpreted by the heterogeneity of the rock material and the different total socket lengths between these two piles. For a more extended socket (TP3), shear stress distributes on the larger shaft surface, and the ultimate side resistance could not be reached for the maximum applied load during testing.

## 4 Numerical Modeling of Pile Load Tests Tp2

The axisymmetric numerical model was composed using Plaxis 2D V20 finite element program (FEM) (Brinkgreve et al. 2017). This approach ignores the presence of reaction piles. However, it can still be considered appropriate due to the relatively large spacing between test and anchor piles (≈ 5D, where D—tests pile diameter) and relatively short test pile length. Additionally, the position of steel sleeves used for reaction piles (embedded below the test pile bottom) contributes to the reduction of the anchor piles' influence on the behavior of the test pile. The details of the numerical models are described for the individual components, which include: the boundary conditions, piles, soil and rock mass, pile-rock mass interface, base conditions, and construction phases, including the loading program.

The experimental and numerical results were compared for the TP2 as this is the only test pile that experienced significant irreversible deformation after surcharge removal. The numerical model is illustrated in Fig. 19, indicating the finite element mesh coarseness and the total number of elements.

Triangular 15 node elements were employed for modeling the soil/rock and concrete piles. Additional details of these modeling approaches were described below, along with the simulation results.

### 4.1 Boundary Conditions

A horizontal (X-direction) restraint boundary was assigned to the right and left sides of the model. The bottom boundary of the model was assumed to be fixed in both the X and

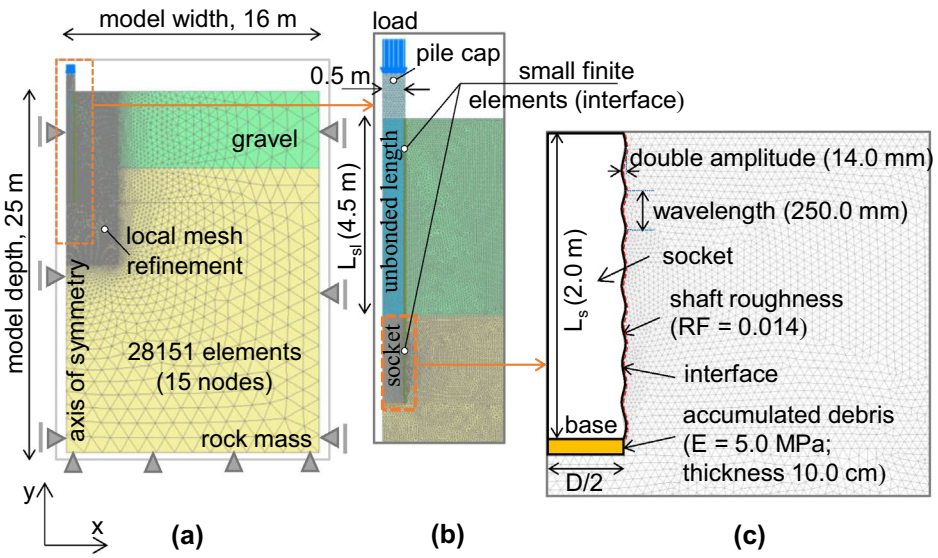


**Fig. 19** Numerical model of test pile 2 (TP2): **a** 2D axisymmetric model; **b** Pile characteristics; **c** Socket details

**Table 4** Material properties for the numerical model

| Parameter | Gravel | Rock mass | Unbonded (sleeved) pile length | Pile socket | Pile cap |
|---|---|---|---|---|---|
| Unit weight, γ [kN/m$^3$] | 16.0 | 23.0 | 25.0 | 25.0 | 25.0 |
| Internal friction angle, φ' [°] | 38.0 | 63.0 | – | – | – |
| Cohesion, c' [kN/m$^2$] | 1.0 | 260.0 | – | – | – |
| Interface reduction factor, $R_i$ [-] | 0.2 | 1.0 | – | – | – |
| Dilatancy angle, ψ [°] | 8.0 | 20.0 | – | – | – |
| Deformation modulus, $E_m$ [GPa] | 0.0525 | 1.5 | 26.9 | 36.7 | 43.3 |
| At-rest lateral earth coefficient, $K_0$ [-] | 0.384 | 1.0 | – | – | – |
| Poisson ratio, ν [-] | 0.3 | 0.25 | 0.25 | 0.25 | 0.25 |

Y directions. A surcharge load was applied incrementally at the top of the test pile to simulate the testing procedure.

## 4.2 Piles

Piles were modeled as a linear elastic solid element in line with the approximation shown in Fig. 19b. Finite element mesh could not be generated for extremely complex measured shaft geometry, so the simplified representative sinusoidal surface was adopted in numerical simulations. Namely, the idealized sinusoidal pile shaft profile was modeled as a sequential reverse curvilinear wave (Fig. 19c). The double wave amplitude equals 14.0 mm, which agrees with the mean roughness height calculated from the field measurements. The selected amplitude resulted in the roughens factor RF = 0.015, measured for TP2. Wavelength equal to 250.0 mm was selected as representative according to the general shape of the roughness measurement profile, noting that this is a specific value used in other studies (Gutiérrez-Ch et al. 2020b). Concrete specimens were collected for unconfined compression testing (3 specimens per pile) and loaded to the failure in the laboratory. The characteristic cylinder compressive strength was determined from the unconfined strength measured 14 days since the piles were tested 14 days after installation. This strength value was later used to determine pile elastic modulus, corresponding to 34 GPa, according to EN (1992).

An average pile elastic modulus ($E_p$) of 36.7 GPa and 40.0 GPa was assigned to the socket and sleeved pile segments, respectively. Such value was calculated using a formula proposed in Zhan and Yin (2000) to estimate the elastic modulus of the composite material of steel and concrete as:

$$E_p = E_c(1 - r) + E_s r \tag{6}$$

where: $E_c$—the elastic modulus of concrete equal to 34.0 GPa, $E_s$—the elastic modulus of steel equal to 205.0 GPa, and r—the percentage of steel (reinforcement or steel sleeve) equals 1.63% and 3.5% for the socket and unbonded (sleeved) segment of piles, respectively.

Since the pile was modeled as a solid element with a diameter of 1.0 m, equivalent values of reference Young's modulus were defined, accounting for its entire surface. These values are indicated in Table 4, showing the input parameters of the numerical model.

Poisson's ratio for rock mass and piles ($\nu_p$) equals 0.25, noting that the variation in Poisson's ratio of rock and concrete within these ranges has minimal effect on the elastic settlement of piles (Pells and Turner 1979).

## 4.3 Soil and Rock Mass

The soil and rock were simulated by using the Mohr–Coulomb constitutive model. The parameters are listed in Table 4. Gravel strength and stiffness parameters were correlated with SPT test results. In contrast, the direct shear laboratory test described in the first part of this paper determined the rock mass strength parameters. Internal friction angle and cohesion were selected to represent linear strength envelope slope and shear stress intercept for the 6.0 mm shear displacements since this value is in the range of pile socket displacements measured for TP2. To account for the non-associated flow rule, the plastic potential function was defined independently from the strength parameters by introducing a dilatancy angle. The selected dilatancy angle was the slope of load vs. vertical displacement of the samples sheared in the direct shear test. Finally, the rock mass deformation modulus was determined by the equation suggested in Palmström and Singh (2001):

$$E_m = 0.2q_u[GPa] = 1.5GPa \tag{7}$$

**Table 5** Main characteristics of analyzed numerical models

| Model No | Side geometry | | Pile base condition | Pile-rock interface strength | |
|---|---|---|---|---|---|
| | Amplitude [mm] | Wavelength [mm] | | Cohesion [kPa] | Friction angle [°] |
| 1 | 7.0 | 250.0 | Solid base | $c_i = c$ | $tg\varphi_i = tg\varphi$ |
| 2 | | | No-base resistance | $c_i = c$ | $tg\varphi_i = tg\varphi$ |
| 3 | | | | $c_i = 0.67c$ | $tg\varphi_i = 0.67tg\varphi$ |
| 4 | | | | $c_i = 0.5\ c$ | $tg\varphi_i = 0.5tg\varphi$ |
| 5 | | | | $c_i = 0.33c$ | $tg\varphi_i = 0.33tg\varphi$ |

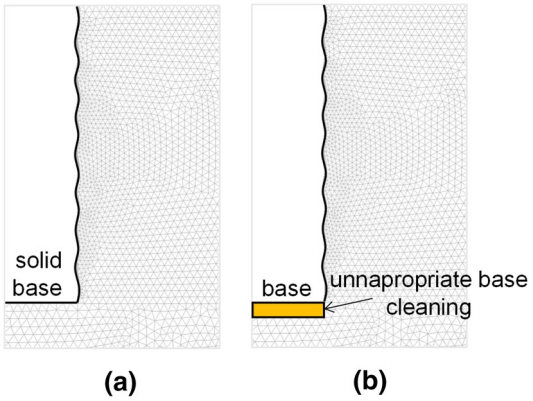


**Fig. 20** Different base conditions assumptions: **a** Solid base; **b** No-base resistance

where: $q_u = 7.5$ MPa is the UCS in [MPa]. A similar value was suggested in Sousa et al. (1997), as cited in the introduction part of the paper.

The unit value of the at-rest lateral earth coefficient ($K_0 = 1.0$) was used to generate initial stress conditions in the rock mass. The same value was suggested in Olalla (2014) since the concrete is very fluid, without any shrinkage when setting in a wet medium, noting that such value is considered the most adequate to represent the stress state of the piles with its shaft submerged. The rock mass tensile strength was neglected by applying the "tension cut off" option with zero tensile strength.

### 4.4 Soil/Rock-Pile Interface

Zero thickness interface elements simulated contact between the sinusoidal pile surface and surrounding material. The details of interface element formulation used in Plaxis 2D V20 software are described in the literature (Brinkgreve et al. 2017; Skejić 2012). Interface elements were defined between pile shaft and soil/rock to account for strength reduction along the pile length (part of pile constructed with a steel sleeve and socketed length). These elements also enable mesh optimization since the mesh dependency is reduced significantly when using interface elements (Tschuchnigg and Schweiger 2013).

The main difference between models analyzed in this study relates to the socket-rock mass contact strength. Unlike the conventional analysis, the strength of the pile-rock interface strength was modeled explicitly by particular material assigned to the interface element and not relatively to surrounding rock strength by introducing the strength reduction factor $R_i \leq 1.0$ on a planar surface. The unit value of the strength reduction factor, $R_i = 1.0$, was selected for rock material. This approach was considered appropriate since the values of $R_i < 1.0$ reduce contact strength and stiffness and introduce the additional parameters that conventional tests can not determine. Additionally, reducing contact stiffness could result in excessive normal displacements on the contact surface. The pile-rock interface along the socket sinusoidal surface was modeled by four different sets of Mohr–Coulomb strength parameters given in Table 5 (Models 2, 3, 4, and 5).

The listed contact strength values were selected to cover the wide range of theoretically assumed values. Dilatancy angle equal to zero was adopted since the rock-socket contact region can dilate due to explicitly modeled undulations.

The strength and stiffness of the sleeved soil-pile length interface were modeled using a reduction coefficient of $R_i = 0.2$ (steel-gravel interface). The value of interface strength along unbonded pile length does not influence the results significantly, so the detailed investigation of this parameter is out of the purpose of this paper.

### 4.5 Base Conditions

Numerical modeling was performed by applying two different assumptions regarding the pile base condition, resulting in two model geometries illustrated in Fig. 20, and specified in Table 5 as follows:

Model 1: The model assuming immediate mobilization of socket base resistance,

Models 2 to 5: The models include the accumulated debris at the pile bottom.

The results of these models will serve to investigate the assumption of a no-base resistance scenario for the TP2, noting that the same parameters of rock mass and socket shaft interface were adopted for this analysis.

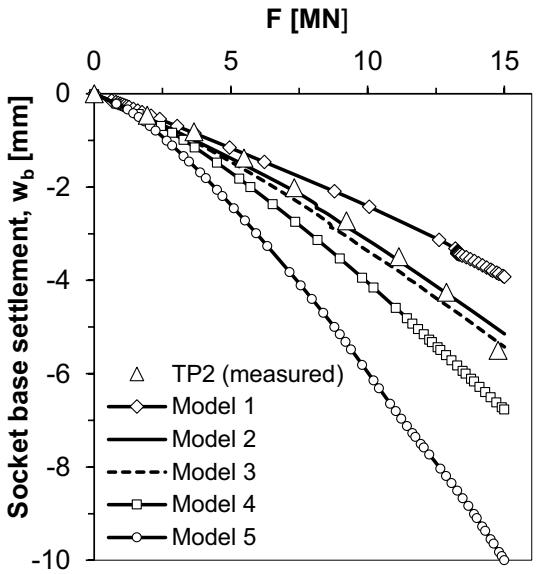


**Fig. 21** Influence of shaft-rock bonding strength on load-pile base settlement response and comparison with measured values

### 4.6 Construction Phases and Loading Program

Construction phases for the numerical models were simulated with respect to the erection of the pile load test (bored piles construction, surcharge load at piles tip). The reload stage has not been included in the numerical analysis.

After the pile installation phase (activation of concrete material), displacements were reset to zero, and the surcharge load was activated. It was applied in a single-phase staged construction procedure as a uniform load on the top of the piles. A sufficient number of additional steps was selected to apply the total loading (circa 100 steps). Incremental, iterative analysis with arc length control was applied (max 60 iterations and tolerated error of 0.01). Consequently, the load was incrementally increased until the maximum applied load was reached.

## 5 Results of the Numerical Modeling and Comparison with Measurements and Empirical Relations

The results for the numerical simulations are presented in three groups (investigation of base/shaft strength influence on pile response-back analysis, comparison with experimental data, and comparisons with empirical relations) in the following subsections.

### 5.1 Base/Shaft-Rock Strength Influence on Pile Response-Back Analysis

Base conditions' influence on pile response was analyzed by comparing results observed for Models 1 and 2. The solid socket base assumption was simulated in Model 1. Applying the maximum load equal to 15.0 MN resulted in 3.9 mm base settlements (see Fig. 21) and the significant mobilization of pile base resistance due to its relatively high stiffness.

The exact values of forces mobilized along the shaft and base were determined by integrating shear and normal stresses along the shaft and base, respectively. The representative cross-section was selected 2.0 cm far from the pile-rock contact surface. The normal stress at the pile base indicates that 30% of the total pile load was supported by the base, which does not agree with observed values during field testing. Contrary, the assumption of shaft socket only was adopted in Model 2 by including the 10.0 cm thick elastic material of relatively low stiffness ($E = 5\,000$ kPa and $\nu = 0.3$) below the pile aiming to simulate the ineffective base cleaning (accumulated debris) before concrete installation. Consequently, it resulted in a 5.1 mm pile base settlement and higher side resistance mobilization. The total load was supported by the socket shaft, which agrees with field observations since zero axial force was measured at the pile base. These results indicate that the accumulated debris below the pile base may be the reason for zero base resistance, suggesting that the strain gauges were operative during the testing.

The influence of shaft-rock strength on the load-settlements curves was analyzed by comparing outcomes for

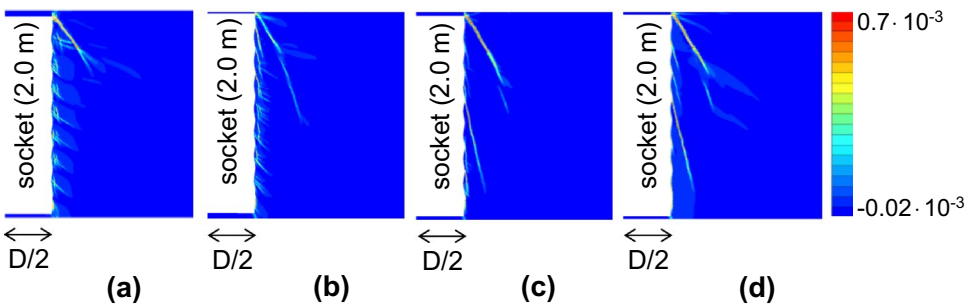


**Fig. 22** Incremental shear strains indicating failure mechanism for **a** Model 5; **b** Model 4; **c** Model 3; **d** Model 2

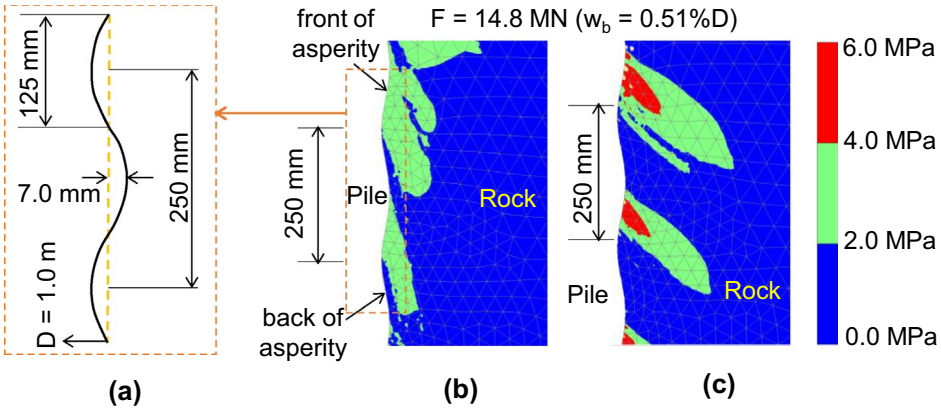


**Fig. 23** **a** Idealized asperity geometry (RF = 0.015); Shear stress ($\sigma_{xy}$) contours near the socket asperities for $F = 14.8$ MN ($w_b = 0.51\%D$): **b** Model 2; **c** Model 5

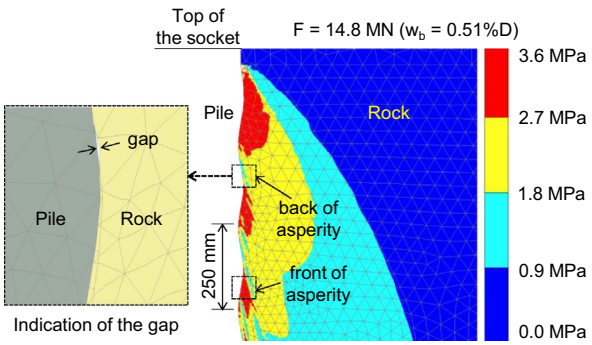


**Fig. 24** Mobilized shear stress around the socket and an indication of the gap at the back of asperity for Model 2 (TP2)

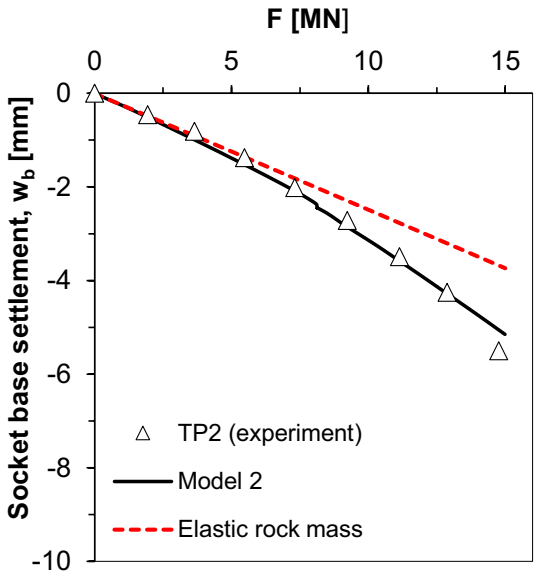


**Fig. 25** Interpretation of difference between numerical model results and measurements

Models 2 to 5. These results were shown in Fig. 21, illustrating comparative data for both the measured and the numerically predicted pile base settlement. The pile base rather than pile cap settlement was selected due to uncertainties with the modeling of the sleeved pile segment. Comparing the actual displacement measured at the pile toe with the numerical simulation confirms that the bond strength plays a significant role in the shear load-transfer characteristics of socketed piles. Incremental shear strains are shown in Fig. 22 for the final load stage, and different failure mechanisms were observed during the simulations.

Namely, maximum shear bands were concentrated near the asperities for models with low bond strength resulting in asperity shorn off (curved failure surface). Similar observations were recorded during small-scale physical modeling that included a 3D deformation analysis system (Xu et al. 2020) mentioned in the introduction, noting that those tests were performed with an aluminum alloy pile. By contrast, maximum shear deformations were distributed considerably from the undulations for Model 2, indicating the failure surface contained two or more undulations. This behavior is related to the shear stress distribution around asperities (see Fig. 23). For low bond strength (Model 5-Fig. 23b), most of the pile load was supported by the front part of the asperities, and significant local shear stress initiated asperity shorn off. The higher bonded strength (Model 2-Fig. 23b) resulted in a more homogenous distribution of shear stress along with the socket. The failure surface was advanced deeper from the pile side in the radial direction.

The mobilized shear stress for F = 14.8 MN, corresponding to the socket base settlement, $w_b = 0.51\%D$, for Model 2 was given in Fig. 24. The locations of minimum mobilized shear stress at the pile-rock interface match the location of the back of asperity, indicating the gap between the pile and rock mass. Contrary, the maximum mobilized shear stress agrees with the location of the front of asperity. A similar distribution of mobilized shear stresses was obtained for other analyzed numerical models in this study, which is comparable with the results obtained by Gutiérrez-Ch (2020c) and Hassan and O'Neill (1997).

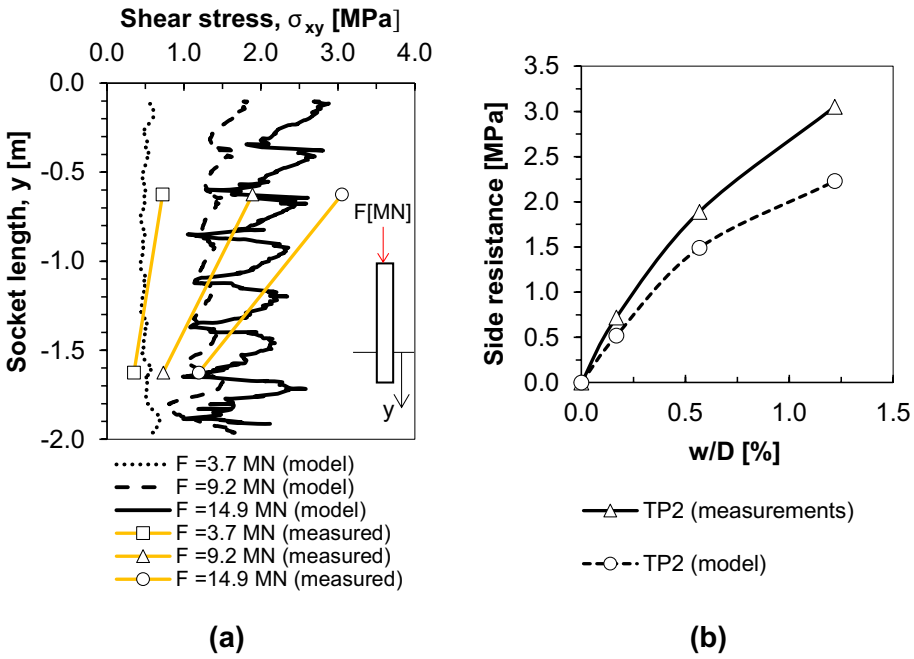


**Fig. 26** Comparison of socket shaft resistance predicted by Model 2 at the three loading stages and comparison with experimental data for TP2: **a** shear stress along with the socket; **b** average shear stress mobilized at the upper portion of the socket (1.25 m length)

## 5.2 Comparison with Experimental Data

To assess whether numerical simulations would also confirm the general features measured during the experimental program of TP2, a comparison between the results will be presented in this section. The best matching between calculated and observed socket settlements was confirmed for Model 2 (see Fig. 21), noting that numerical results do not fully reproduce the observed behavior. Aiming to illustrate the error percentage, Model 2 results were shown along with measured data in Fig. 25.

For instance, for a pile base settlement less than 0.5 to 1.0 mm, the axial loads are about 10% to 20% lower for Model 2 than its corresponding field test (the calculated settlement was overpredicted). Additionally, for the socket base settlements higher than 4.5 mm, a total mobilized force from the numerical model indicated a stiffer response than the field test's response (the calculated settlements were underpredicted). After this displacement, the obtained load settlement curve suggests that Model 2 will have more load capacity than field tests. Aiming to explain this issue, the response of the pile in the elastic medium is illustrated in Fig. 24 by the dotted line. Generally, for the socket base settlements ($w_b$) less than 1.2 mm ($w_b/D = 0.12\%$), the observed pile response follows the pile-settlement curve obtained by assuming the linear elastic rock material and shaft-rock contact. On the contrary, a less stiff response resulting in a lower mobilized load for the same displacement ($w_b = 1.2$ mm) resulted from Model 2. This is attributed to plastic deformations in the rock mass around the socket after the stress state reached the peak strength envelope. However, such behavior was expected since the representative strength parameters were selected for mobilized shear stress lower than peak values measured in the direct shear test. As reported in Sect. 2.3 (see Fig. 6), peak strength was reached at approx 1.5 mm shear displacement for the representative normal stress range.

This agrees well with the critical settlement corresponding to the starting point of measurements and elastic model deviation. It is expected that a numerical model which includes peak and critical strength parameters rather than only one set of equivalent values of cohesion and internal friction angle would result in better agreement with observed load-settlement behavior.

An indication of shear stress mobilization with surcharge load increment was given in Fig. 26a.

The absolute values of shear stresses around the socket were illustrated for three representative phases of a pile load test. The distribution of shear stress along with the socket from the numerical simulation is generally uniform when compared with experimental data. However, the distribution of shear stress mobilized at 2.0 cm distance from sinusoidal socket surface captures the tendency of shear stress reduction from the top to the central part of the socket. The numerically obtained average side resistance (for total socket length) at maximum pile head load (F = 14.9 MN) equals 2.05 MPa, which is 16% lower than measured on-site for TP2. The average shear stress mobilized in the upper portion of the socket (1.25 m length) illustrates the difference between measurement and simulation (Fig. 26b). These reasonably good shear stress estimates were obtained for lower load levels, noting that the discrepancy generally becomes

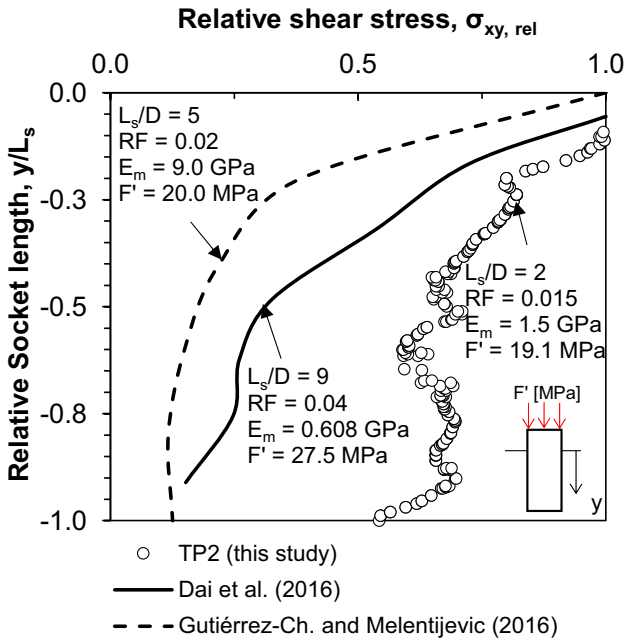


**Fig. 27** Comparison of FEM results with similar numerical studies from the literature

more evident as the surcharge load increases. This difference may be attributed to the relatively simple rock mass model that excludes the strain-softening similar to the load-settlement discrepancy discussion.

Finally, the results in Fig. 27 compare relative shear stress ($\sigma_{xy}/\sigma_{xy,\,max}$) distribution along with the socket ($y/L_s$) with similar studies from the literature (Dai et al. 2016; Gutiérrez-Ch and Melentijevic 2016). A typical cross-section for shear stresses comparison was defined at a 10.0 cm distance from the socket, similar to Gutiérrez-Ch and Melentijevic (2016). Some differences were recognized in the shear stress reduction rate, which may be attributed to different socket geometries analyzed in the present study. Moreover, the surcharge load ($F' = F/A_p$ in [MPa]) and rock mass characteristics differed considerably from referenced results. However, two shear stress peaks, near the top and bottom of the socket, with the lower being less noticeable, were obtained similar to numerical FEM results (Dai et al. 2016) and centrifuge small-scale model results (Gutiérrez-Ch et al. 2021b).

These numerical results indicate that satisfactory modeling of relative displacement between the pile and surrounding rock mass is possible on the basis of a linear elastic solid pile element with sinusoidal undulations and its equivalent strength at the interface with the rock. However, due to different uncertainties in selecting reference stiffness and strength parameters, slippage of the elastic pile relative to the rock mass followed by incremental mobilization of shaft resistance should be modeled more appropriately to gain a more realistic displacement field. The load settlement response and pile base resistance mobilization of TP2 predicted by the numerical Model 2 does, however, agree well with experimental observation.

## 6 Conclusion

This paper presents the experimental and numerical analysis of static load tests performed on axially loaded socket piles in a conglomerate rock mass. The measurements collected during testing of one selected pile (TP2) were compared against the numerical simulations with different model assumptions, noting that independent measurements determined socket roughness and shear strength parameters of conglomerate rock. The load-settlement behavior predicted by numerical simulations agrees well with the actual measurements, while generally, the numerical model results improve the interpretations.

Based on the results of this study, the following conclusions are drawn:

- The unconfined compression strength (determined on relatively small intact specimens) and measured roughness (obtained for pile core surface) are valuable data for predicting the ultimate bearing capacity of socketed piles. Namely, the UCS values were used for predicting the ultimate average side resistance by advanced empirical formulations, including roughness data input. Estimated side resistance for particular methods was close to measurements. At the same time, some deviated significantly, noting that the average measured ultimate side resistance for the shaft-only socket that reached the ultimate stage (TP2) was generally higher than predicted.
- The reported full-scale field tests can serve as a benchmark for verifying empirical models for piles of the relevant type. Testing results indicate that even for relatively short socket length, the poorly cemented conglomerate ($5.0\ \text{MPa} < q_u < 10.0\ \text{MPa}$) can sustain a heavy surcharge before settlements indicating the commencement of full slip were reached. A relatively rough pile shaft surface resulted in most of the load being attracted by the upper part of the socket. These findings support the results obtained by centrifuge tests, especially for rough sockets, adding great value to understanding the behavior of rock-socketed piles. Moreover, due to high rock mass stiffness and strength, it is observed that significant bond strength is mobilized at small displacements ($w/D < 1.0\%$).
- An increment in socket length resulted in decreased pile-rock relative displacements, and the mobilized axial load distribution along the pile became more gradual for a given pile head load. These findings represent the socket

behavior for lower pile settlements (w/D < 1%) reached during testing.

- The FEM back-analysis results indicate that pile-shaft contact strength equals the rock mass strength (Model 2 is the best-calibrated model). The average side resistance obtained by numerical modeling for TP2 was comparable (16% lower) to the average side resistance mobilized for maximum pile head load during full-scale testing. The numerical results generally tend to agree with the overall trends measured during the field test and small-scale physical models (1 g and centrifuge test results). However, some local-level differences were recognized, indicating that asperities included in the FEM model geometry are insufficient to reproduce all aspects of complex pile-rock interaction.

Even though the relatively short socket lengths were adopted in the present study, future research on a similar topic should include the tests on even more shortened socket lengths. Consequently, displacements indicating full slip at pile-rock interface could be reached on total socket length, and a particular value of ultimate average side resistance could thus be obtained. The scanned asperity height measured on the pile core corresponds to the values representative of the standard drilling tool without artificial roughening. However, a challenging direct measurement of shaft roughness along the socket drillhole could provide more relevant results than those presented in this study, where shaft surface and pile core geometry were assumed to be equal.

**Acknowledgements** The pile testing program was implemented as part of construction works performed during the erection of the "Počitelj" bridge provided by a public company, Motorways of the Federation of Bosnia and Herzegovina. The pile load tests were performed at the initiative of the IPSA Institute, while the investigation works and the piles testing were performed by the Hering company supported by the Geo konzalting, Winner Project, Geoinvest and the faculty of Mechanical Engineering Mostar. The laser scanning measurements were completed by the Geobiro company, while the direct shear testing was organized at the faculty of Civil Engineering in Sarajevo. The authors express their deep gratitude for unrestricted access during the investigation works and in situ testing and collaboration with all parties involved.

## References

ASTM D5607–02 (2008). Standard test method for performing laboratory direct shear strength tests of rock specimens under constant normal force.

ASTM International. (2013). *Standard test method for deep foundations under static axial compressive load*. ASTM International.

Alnuaim AM, Hamid WM, Alshenawy AO (2020) Numerical study of skin friction behavior of piles in limestone rock. Soil Mech Found Eng 57(3):265–269

Alrifai L (2007) Rock socket piles at mall of the emirates, Dubai. Proc Inst Civ Eng Geotech Eng 160(2):105–120

Asem P, Gardoni P (2019) Evaluation of peak side resistance for rock socketed shafts in weak sedimentary rock from an extensive database of published field load tests: a limit state approach. Can Geotech J 56(12):1816–1831

Akram, M. S., Sharrock, G., & Mitra, R. (2010). *Physical and numerical investigation of conglomeratic rocks* (Doctoral dissertation, Ph. D. Thesis, University of New South Wales, Sydney, Australia).

Akgüner C, Kirkit M (2012) Axial bearing capacity of socketed single cast-in-place piles. Soils Found 52(1):59–68

Barbalić I, Galjan B, Bandić M, Ivandić K (2007) Pile testing at the Dubrovnik passenger port construction site. Građevinar, 59(08.):693–703.

Basarkar SS, Dewaikar DM (2006) Load transfer characteristics of socketed piles in Mumbai region. Soils Found 46(2):247–257

Benmokrane B, Mouchaorab KS, Ballivy G (1994) Laboratory investigation of shaft resistance of rock-socketed piers using the constant normal stiffness direct shear test. Can Geotech J 31(3):407–419

Bieniawski ZT, Van Heerden WL (1975) The significance of in situ tests on large rock specimens. International Journal of Rock Mechanics and Mining Sciences & Geomechanics Abstracts (Vol. 12, No. 4, pp. 101–113). Pergamon.

Brinkgreve RBJ, Engin E, Swolfs WM (2017) Plaxis 2D manual. *Rotterdam, Netherlands, Balkema*.

Carrubba P (1997) Skin friction on large-diameter piles socketed into rock. Can Geotech J 34(2):230–240

Chen XY, Zhang MY, Bai XY (2018) Axial resistance of bored piles socketed into soft rock. KSCE J Civ Eng 23(1):46–55

Cheng F, Haberfield CM, Seidel JP (1996). Laboratory study of bonding and wall smear in rock socketed piles. In: 7th Australia New Zealand conference on geomechanics: geomechanics in a changing world: conference proceedings (p. 69). Institution of Engineers, Australia.

Dai G, Salgado R, Gong W, Zhu M (2016) The effect of sidewall roughness on the shaft resistance of rock-socketed piles. Acta Geotech 12(2):429–440

Dykeman P, Valsangkar AJ (1996) Model studies of socketed caissons in soft rock. Can Geotech J 33(5):747–759

Eid HT, Bani-Hani K (2012) Settlement of axially loaded piles entirely embedded in rock-analytical and experimental study. Geomech Geoeng 7(2):139–148

Eid HT, Shehada AA (2013) Estimating the elastic settlement of piled foundations on rock. Int J Geomech 15(3):0401405

EN (1992). 1–1: 2004 Eurocode 2: Design of concrete structures. General rules and rules for buildings, 1992–3.

Ervin MC, Finlayson JE (2006) Piled foundations for Eureka Tower, Melbourne, Australia. Proc Inst Civ Eng-Geotech Eng 159(3):187–194

Fellenius, B. (2017). *Basics of foundation design*. Lulu.com.

Gutiérrez-Ch JG, Melentijevic S (2016) Análisis numérico del efecto de la rugosidad en el contacto pilote-roca sobre la resistencia por fuste y punta. Revista Digital Del Cedex 182:41–41

Gutiérrez-Ch JG, Melentijevic S, Senent S, Jimenez R (2019) DEM models to predict side shear resistance of rock-socketed piles considering socket roughness. In: 53rd US rock mechanics/geomechanics symposium. American Rock Mechanics Association.

Gutiérrez-Ch JG, Senent S, Melentijevic S, Jimenez R (2021a). A DEM-based factor to design rock-socketed piles considering socket roughness. Rock Mechanics and Rock Engineering, 1–13.

Gutiérrez-Ch JG, Song G, Heron C, Marschall A, Jimenez R (2020a) Centrifuge modelling of shaft resistance of a rock-socketed pile. Proceeding 4th european conference on physical modelling in geotechnics-ECPMG, 06–08 September, Lulea, Sweden.

Gutiérrez-Ch JG, Melentijevic S, Senent S, Jimenez R (2020b) Distinct-element method simulations of rock-socketed piles: estimation of side shear resistance considering socket roughness. J Geotech Geoenviron Eng 146(12):04020133

Gutiérrez-Ch JG (2020c) Análisis del efecto de la rugosidad en el contacto roca-pilote sobre la resistencia por fuste de pilotes. [In Spanish.] Ph.D. thesis, Ingeniería y Morfología del Terreno, Universidad Politécnica de Madrid. https://doi.org/10.20868/UPM.thesis.63589.

Gutiérrez-Ch JG, Song G, Heron CM, Marshall A, Jimenez R (2021b) Centrifuge tests on rock-socketed piles: effect of socket roughness on shaft resistance. J Geotech Geoenviron Eng 147(11):04021125

Haberfield CM, Lochaden ALE (2019) Analysis and design of axially loaded piles in rock. J Rock Mech Geotech Eng 11(3):535–548

Hassan KM, O'Neill MW (1997) Side load-transfer mechanisms in drilled shafts in soft argillaceous rock. J Geotech Geoenviron Eng 123(2):145–152

Hoek E, Brown ET (1997) Practical estimates of rock mass strength. Int J Rock Mech Min Sci 34(8):1165–1186

Horvath RG (1982) Behaviour of rock-socketed drilled pier foundations (Doctoral dissertation, Ph. D. Thesis, University of Toronto, Toronto).

Horvath RG, Kenney TC, Trow WA (1980) Results of tests to determine shaft resistance of rock-socketed drilled piers. In: International Conference on Structural Foundations on Rock, 1980, Sydney, Australia (Vol. 1).

Horvath RG, Kenney TC, Kozicki P (1983) Methods of improving the performance of drilled piers in weak rock. Can Geotech J 20(4):758–772

ICE Specification for Piling and Embedded Retaining Walls. (2016), ICE Publishing, Third Edition, 21–216.

International Society for Rock Mechanics (1978) Suggested methods for determining uniaxial compressive strength and deformability of rock materials, ISRM Committee on Standardization of Laboratory Tests. Int J Rock Mech Min Sci 16:137–140

Kaderabek TJ, Reynolds RT (1981) Miami limestone foundation design and construction. J Geotech Eng Div 107(7):859–872

Kirkit M, Kılıç H, Akgüner C (2010) Numerical analyses of axial load capacity of rock socketed piles in Turkey. In: Numerical Methods in Geotechnical Engineering (pp. 665–670). CRC Press.

Kong KH, Kodikara J, Haque A (2006) Numerical modelling of the side resistance development of piles in mudstone with direct use of sidewall roughness. International journal of rock mechanics and mining sciences (1997), 43(6), 987–995.

Kou HL, Guo W, Zhang MY, Xu YQ (2016) Axial resistance of long rock-socketed bored piles in stratified soils. Ocean Eng 114:58–65

Kulhawy FH, Phoon KK (1993) Drilled shaft side resistance in clay soil to rock. Design and performance of deep foundations: Piles and piers in soil and soft rock, (pp. 172–183). ASCE.

Krsmanović D (1967) Initial and residual shear strength of hard rocks. Geotechnique 17(2):145–160

Leung CF, Ko HY (1993) Centrifuge model study of piles socketed in soft rock. Soils Found 33(3):80–91

Mahmoud AM, Samieh AM (2017) Displacement assessment of rock socketed shafts: a numerical approach. In: International congress and exhibition" sustainable civil infrastructures: innovative infrastructure geotechnology (pp. 238–249). Springer, Cham.

Melentijevic S, Olalla C (2014) Different FEM models for simulation of the Osterberg load test in rock shafts. In: Proc. ISRM Regional Symposium-EUROCK 2014. Vigo, pp. 775–781: International Society for Rock Mechanics and Rock Engineering.

Ng CW, Yau TL, Li JH, Tang WH (2001) Side resistance of large diameter bored piles socketed into decomposed rocks. J Geotech Geoenviron Eng 127(8):642–657

Olalla, C. (2014). Foundations on rock masses. In *ISRM Regional Symposium-EUROCK 2014, Vigo, Spain*. International Society for Rock Mechanics and Rock Engineering.

Omer JR, Delpak R, Robinson RB (2002) Instrumented load tests in mudstone: pile capacity and settlement prediction. Can Geotech J 39(6):1254–1272

Palmström A, Singh R (2001) The deformation modulus of rock masses-comparisons between in situ tests and indirect estimates. Tunn Undergr Space Technol 16(2):115–131

Pells PJN, Turner RM (1979) Elastic solutions for the design and analysis of rock-socketed piles. Can Geotech J 16(3):481–487

Pells PJ, Rowe RK, Turner RM (1980) An experimental investigation into side shear for socketed piles in sandstone. International Conference on Structural Foundations on Rock, Sydney, Australia (Vol. 1).

Rahman S, Siddiqui S, Sharp K (2019) Behavior of rock-socketed drilled shaft under uni-axial loading-a parametric study. In: GeoCongress 2019: Foundations (pp. 213-222). Reston, VA: American Society of Civil Engineers

Rezazadeh S, Eslami A (2017) Empirical methods for determining shaft bearing capacity of semi-deep foundations socketed in rocks. J Rock Mech Geotech Eng 9(6):1140–1151

Rosenberg P, Journeaux NL (1976) Friction and end bearing tests on bedrock for high capacity socket design. Can Geotech J 13(3):324–333

Rowe RK, Armitage HH (1984) The design of piles socketed into weak rock. University of Western Ontario, Faculty of Engineering Science

Rowe RK, Armitage HH (1987) A design method for drilled piers in soft rock. Can Geotech J 24(1):126–142

Russo G (2012) Experimental investigations and analysis on different pile load testing procedures. Acta Geotech 8(1):17–31

Seidel JP, Collingwood B (2001) A new socket roughness factor for prediction of rock socket shaft resistance. Can Geotech J 38(1):138–153

Seol HI, Jeong SS (2007) Shaft resistance characteristics of rock-socketed drilled shafts based on pile load tests. J Korean Geotech Soc 23(9):51–63

Seychuk JL (1970) Load tests on bedrock. Can Geotech J 7(4):464–470

Skejić A (2012) Interface formulation problem in geotechnical finite element software. Electron J Geotech Eng 17:2035–2041

Sousa LR, He M, Kanji M (2020) Soft rock mechanics and engineering. Springer

Sousa LR, Nakamura A, Yoshida H, Yamaguchi Y, Kawasaki M, Satoh H. (1997). Evaluation of the deformability of rock masses for dam foundations. Analysis of deformability investigation results of heterogeneous bedrock. Technical Memorandum of PWRI, no. 3514, Tsukuba City, 45p.

Šunjić G, Džeba T, Prskalo M (2020) Geotechnical characteristics of the banks in the middle course of the Neretva River through the City of the Mostar. e-Zbonik: Electronic collection of papers of the Faculty of Civil Engineering, (20).

Thorburn S (1966) Large diameter piles founded on bedrock. In: Large Bored Piles (pp. 121–129). Thomas Telford Publishing.

Turner JP (2006) Rock-socketed shafts for highway structure foundations (Vol. 360). Transportation Research Board.

Tschuchnigg F, Schweiger HF (2013) Comparison of deep foundation systems using 3D finite element analysis employing different modeling techniques. Geotech Eng J SEAGS & AGSSEA 44(3):40–46

Vu TT (2013) Load and resistance factor design of drilled shafts at the service limit state (Doctoral dissertation, University of Missouri-Columbia).

Wang TH, Zhang L, Hao YZ, Jin X (2020) Side Friction of Rock-Socketed Piles Involving Thick Sediment. Adv Civ Eng 2020.

Williams AF (1980) The design and performance of piles socketed into weak rock.

Williams AF, Johnston IW, Donald IB (1980) The design of socketed piles in weak rock. International conference on structural foundations on rock, 1980, Sydney, Australia (Vol. 1).

Williams A, Pells PJN (1981) Side resistance rock sockets in sandstone, mudstone, and shale. Can Geotech J 18(4):502–513

Wood DM (2003) Geotechnical modelling (Vol. 1). CRC press.

Xu J, Haque A, Gong W, Gamage RP, Dai G, Zhang Q, Xu F (2020) Experimental study on the bearing mechanisms of rock-socketed piles in soft rock based on micro X-ray CT analysis. Rock Mech Rock Eng 53(8):3395–3416

Xu J, Dai G, Gong W, Zhang Q, Haque A, Gamage RP (2020b) A review of research on the shaft resistance of rock-socketed piles. Acta Geotechnica, 1–25.

Yong LEI, Yin JF, Chen QN, Liu YX (2017) Experimental study on the rock-socketed segment of pile and analysis of its load-bearing characteristics. J Highway Trans Res Dev 11(3):54–61

Zlatar M (2008) Calculating the capacity of bored piles using test loads. International Conference Civil Engineering-Science and Practice, GNP, Žabljak, Montenegro, 559–564.

Zhan C, Yin JH (2000) Field static load tests on drilled shaft founded on or socketed into rock. Can Geotech J 37(6):1283–1294

Zhang L, Einstein HH (1998) End bearing capacity of drilled shafts in rock. J Geotech Geoenviron Eng 124(7):574–584

Zhou J, Zhou C, Feng Q, Gao T (2020) Analytical model for load-transfer mechanism of rock-socketed drilled piles: considering bond strength of the concrete–rock interface. Int J Geomech 20(6):04020059

Zuo G, Drumm EC, Islam MZ, Yang MZ (2004) Numerical analysis of drilled shaft O-cell testing in mica schist. In: GeoSupport 2004: Drilled Shafts, Micropiling, Deep Mixing, Remedial Methods, and Specialty Foundation Systems (pp 778–789).